2021

A Computational Approach To The Study Of Trauma

Evangelos Tsiklidis
University of Pennsylvania

A Computational Approach To The Study Of Trauma

Abstract

Trauma with hypovolemic shock is an extreme pathological state that challenges the body to maintain blood pressure and oxygenation in the face of hemorrhagic blood loss. In conjunction with surgical actions and transfusion therapy, survival requires the patient's blood to maintain hemostasis to stop bleeding. The physics of the problem are multiscale: (1) the systemic circulation sets the global blood pressure in response to blood loss and resuscitation therapy, (2) local tissue perfusion is altered by localized vasoregulatory mechanisms and bleeding, and (3) altered blood and vessel biology resulting from the trauma as well as local hemodynamics control the assembly of clotting components at the site of injury. Building upon ongoing modeling efforts to simulate arterial or venous thrombosis in a diseased vasculature, we have developed models of trauma (both multiscale and machine-learning based) to understand patient risk and predict response. Key results were: (1) the upstream vascular network rapidly depressurizes to reduce blood loss, (2) wall shear rates at the hemorrhaging wound exit are sufficiently high (~10,000 s-1) to drive von Willebrand Factor unfolding, (3) full coagulopathy results in >2L blood loss in 2 hours for severing all vessels of 0.13 to 0.005 mm diameter within the bifurcating network, whereas full hemostasis limits blood loss to <100 mL within 2>min, and (4) hemodilution from transcapillary refill increases blood loss and could be implicated in trauma induced coagulopathy. Machine learning based methods were also implemented to understand trauma patient outcomes. A 400-estimator gradient boosting classifier was trained to predict survival probability and the model is able to predict a survival probability for any trauma patient and accurately distinguish between a deceased and survived patient in 92.4% of all cases. Partial dependence curves (Psurvival vs. feature value) obtained from the trained model revealed the global importance of Glasgow coma score, age, and systolic blood pressure while pulse rate, respiratory rate, temperature, oxygen saturation, and gender had more subtle single variable influences. Shapley values, which measure the relative contribution of each of the 8 features to individual patient risk, were computed for several patients and quantified patient-specific warning signs.

Degree Type

Dissertation

Degree Name

Doctor of Philosophy (PhD)

Graduate Group

Chemical and Biomolecular Engineering

First Advisor

Scott L. Diamond

Second Advisor

Talid Sinno

Keywords

TRAUMA

Subject Categories

Biomedical

A COMPUTATIONAL APPROACH TO THE STUDY OF TRAUMA

Evan Tsiklidis

A DISSERTATION

in

Chemical and Biomolecular Engineering

Presented to the Faculties of the University of Pennsylvania

in

Partial Fulfillment of the Requirements for the

Degree of Doctor of Philosophy

2021

Supervisor of Dissertation

_____

Scott L. Diamond

Professor, Chemical and Biomolecular Engineering

Co-Supervisor of Dissertation

_____

Talid Sinno

Professor, Chemical and

Biomolecular Engineering

Graduate Group Chairperson

_____

John Crocker, Professor Chemical and Biomolecular Engineering

Dissertation Committee

John Crocker Professor, Chemical and Biomolecular Engineering

Paris Perdikaris, Assistant Professor, Mechanical Engineering and Applied Mechanics

A COMPUTATIONAL APPROACH TO THE STUDY OF TRAUMA

Dedication page

In loving memory of my grandfather, Evan Bounatsos. I love and miss you.

ACKNOWLEDGMENT

First and foremost, I would like to thank my advisors Scott L. Diamond and Talid Sinno. It was a tremendous honor to learn from both of you and I always valued our discussions. I feel privileged to have been a student of these great advisors and I valued every moment of our discussions regarding the direction of my research.

I would also like to thank my committee members, Dr. Paris Perdikaris and Dr. John Crocker. Their constructive criticism of my research expanded the horizon of the project.

Next, I thank my lab group members. Working besides very intelligent and friendly students made research infinitely times more enjoyable. This is especially true of the members that I saw extensively on the 5th floor of Vagelos: Yichen Lu, Jifu Tan, Abbas Fakhari, Noelia Grande Gutierrez, and Kaushik Shankar– I thank you all for our meaningful discussions. Jason Rossi, Chris Verni, and Mike Decortin – although you all are Boston Red Sox fans, it was a privilege to work with all of you.

Lastly, I would like to thank my friends outside of the lab who have enriched my life. This includes Jaden Daubert, Wala Kortue, Manasvita Vashisth, Katie Rose, Luke Johnson, Jeff Wang, Adam Suppes, Elliot Haden, Steven Solis, Brian Rich, Amberly Mendes, Evalyn Hart, Aisha Popoola, Brielle Okulicz and many more. Thank you all for creating some of my fondest graduate school memories. I would also like to thank my friends in the Philadelphia Greek Basketball League, playing basketball with my teammates made my graduate school years much more enjoyable.

Finally, I would like to thank my family. My parents and two brothers supported my decision to attend graduate school and were always unwavering in their support. I also appreciate the sacrifices that my parents made to ensure that I had great educational opportunities throughout my life.

ABSTRACT

A COMPUTATIONAL APPROACH TO THE STUDY OF TRAUMA

Evan Tsiklidis

Talid Sinno, Scott L. Diamond

Trauma with hypovolemic shock is an extreme pathological state that challenges the body to maintain blood pressure and oxygenation in the face of hemorrhagic blood loss. In conjunction with surgical actions and transfusion therapy, survival requires the patient's blood to maintain hemostasis to stop bleeding. The physics of the problem are multiscale: (1) the systemic circulation sets the global blood pressure in response to blood loss and resuscitation therapy, (2) local tissue perfusion is altered by localized vasoregulatory mechanisms and bleeding, and (3) altered blood and vessel biology resulting from the trauma as well as local hemodynamics control the assembly of clotting components at the site of injury. Building upon ongoing modeling efforts to simulate arterial or venous thrombosis in a diseased vasculature, we have developed models of trauma (both multiscale and machine-learning based) to understand patient risk and predict response. Key results were: (1) the upstream vascular network rapidly depressurizes to reduce blood loss, (2) wall shear rates at the hemorrhaging wound exit are sufficiently high (~10,000 s^{-1}) to drive von Willebrand Factor unfolding, (3) full coagulopathy results in >2L blood loss in 2 hours for severing all vessels of 0.13 to 0.005 mm diameter within the bifurcating network, whereas full hemostasis limits blood loss to <100 mL within 2 min, and (4) hemodilution from transcapillary refill increases blood loss and could be implicated in trauma induced coagulopathy. Machine learning based methods were also implemented to understand

trauma patient outcomes. A 400-estimator gradient boosting classifier was trained to predict survival probability and the model is able to predict a survival probability for any trauma patient and accurately distinguish between a *deceased* and *survived* patient in 92.4% of all cases. Partial dependence curves ($P_{survival}$ vs. feature value) obtained from the trained model revealed the global importance of Glasgow coma score, age, and systolic blood pressure while pulse rate, respiratory rate, temperature, oxygen saturation, and gender had more subtle single variable influences. Shapley values, which measure the relative contribution of each of the 8 features to individual patient risk, were computed for several patients and quantified patient-specific warning signs.

TABLE OF CONTENTS

LIST OF TABLES

LIST OF ILLUSTRATIONS

CHAPTER 1 Introduction

1.1 Trauma Overview

Modeling the human body's response to acute hemorrhage and tissue trauma requires an understanding of the microscopic level mechanistic steps of blood coagulation, as well as of the global hemodynamic response to the loss of blood volume. The combination of hypovolemic shock and tissue damage creates the greatest risk of **trauma induced coagulopathy (TIC)** where excessive bleeding is difficult to manage. Numerous pathways interact to contribute to TIC including: endothelial dysfunction, unregulated inflammation, NETosis, complement activation, fibrinolysis, consumptive coagulopathy, impaired thrombin production, and hypofunctional platelets (1–3).

About a quarter of trauma patients display a coagulopathy that greatly increases the risk of death. TIC leaves certain patients at risk for uncontrolled bleeding and "oozing", a trait often observed by trauma surgeons. The most immediate biochemical changes driven by blood loss are hypothermia, acidosis, tissue hypoxia, and hypotension. Low pH, low temperature, and low oxygen are all linked to deficient coagulation function (4,5).

Blood pressure and blood loss. At the whole-body scale, the systemic circulation seeks

to compensate for blood loss by several mechanisms. Transcapillary fluid shift draws waterfrom the interstitial space to compensate for the first 0.5 to 1 L of blood loss, a beneficial effect that is attenuated in the dehydrated patient (6). Similarly, the baroreflex modulates cardiac output with declining arterial blood pressure (7). Slower changes in pressure and volume control involve the hypothalamo-pituitary-adrenal (HPA) axis which may be perturbed by traumatic brain injury (TBI) or during shock (8). Modeling efforts described in Section 1 are focused on relating the systemic arterial blood pressure, heart rate, and stroke volume to the amount of blood lost via progressing hemorrhage.

Pressure distributions in damaged vascular networks. At an intermediate length scale of damaged tissue (Section 2), the pressure along a branching arterial or venous network must account for the far upstream pressure condition set by the systemic circulation. The flow through a damaged vessel is different from that of an intact vessel since downstream resistance is lost when a vessel is severed. Specifically, damaged arterial vessels that are bleeding will not be able to maintain high internal pressures since they are directly connected to low pressure environments (P_{atm} or ~10 mm-Hg (interstitial) or -10 mm-Hg in certain diaphragm cavities below atmospheric pressure). The propagation of a vasoconstriction response to mechanical wounding may have significant effect on bleeding. Damage to veins can prevent filling, allowing for depressurization and leading to some back-drainage and diameter collapse. Blood leakage following damage to capillary beds can be regulated in part by smooth muscle cell contraction of precapillary sphincters.

An important attribute of tissue damage to quantify is the instantaneous rate of blood loss relative to the healthy tissue perfusion rate prior to damage.

Changes in blood biology that result in local bleeding. At the molecular and cellular length scale of vessel damage (Section 3), blood loss is controlled by the instantaneous intravascular pressure, the evolving geometry of the wound and the hemostatic action of clotting, and the extravascular pressure. Distinct from thrombosis in a diseased vessel that is not bleeding, hemostasis requires the rapid and controlled assembly of a clot where flowing blood may either leave the vascular space or continue past the wounded region, depending upon the size of damage. Dysfunction of platelets and thrombin generation and hyperfibrinolysis and increased vascular permeability all increase the risk of a situation where blood clots may be insufficient to support hemostasis. Fortunately, the availability of human blood samples has made it possible to assemble a large database of information related to the kinetics, mechanistic steps, initial conditions, and transport influences of blood coagulation and clot formation. Such blood samples are now obtained routinely from trauma patients, for research and diagnostic purposes, for predicting risk, or for informing transfusion choices (eg. plasma vs. platelets vs. RBC).

Shown in Fig 1-1 is a summary of the intricate and complex couplings between blood, vessels, heart, and therapeutic intervention that make TIC difficult to simulate, particularly for impacting real time clinical actions. The research field is at an early stage of creating

well-annotated patient data sets where hospital monitoring information (HR, BP, O2, pH, T, etc) are coupled with clinical laboratory data (pH, CBC, aPTT, blood gases and ions, etc.) and linked with research data (genome sequences, coagulation and platelet phenotyping data) for each patient. Unique to trauma as a disease state, the onset time of trauma (t = 0) is well defined, which may help modeling efforts. However, a challenge for computer modeling of trauma is that the extent of initial traumatic injury, cumulative blood loss, and interstitial water level are difficult to quantify or monitor.

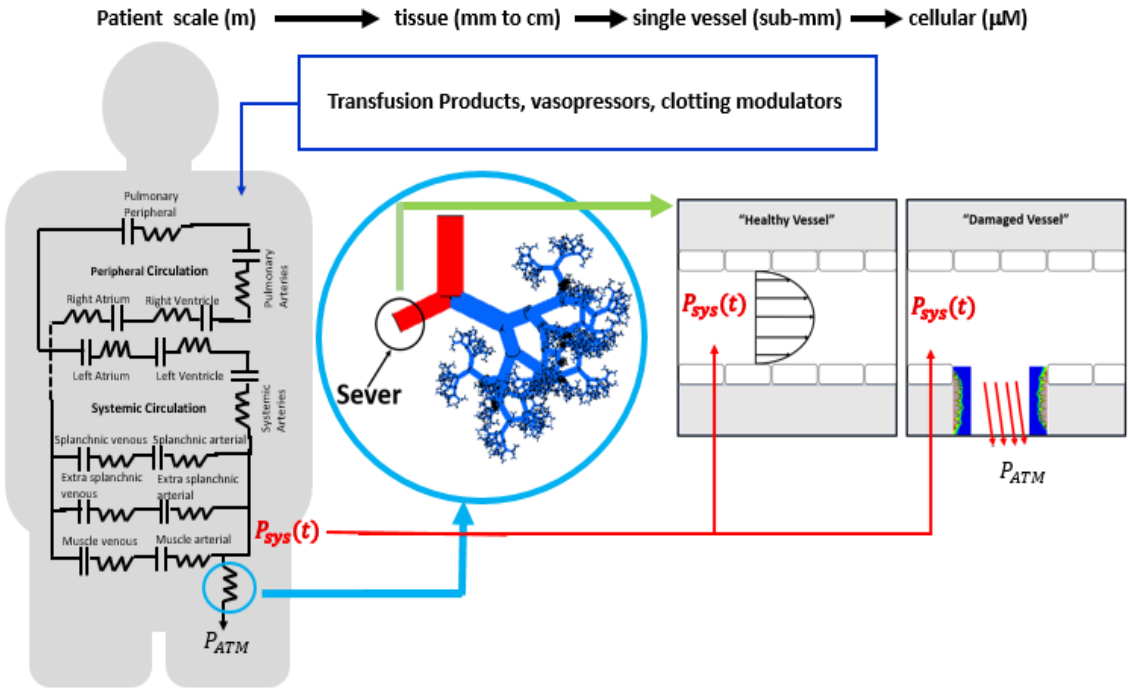

Fig. 1-1 Multiscale Modeling of Trauma patient over 6 orders of magnitude. The global hemodynamics model is typically represented as a closed-loop hydraulic circuit that includes lumped, 0-D, descriptions of the various components of the body. Bleeding can be included in these models by connecting the circuit to atmospheric pressure through a "resistance-to-hemorrhage" resistor, as is done in the Reisner-Heldt model (6). At this scale, cardiovascular output is primarily

modulated by the baroreflex and transcapillary fluid shifts. At the tissue level scale (cm), vasculature branching networks are constructed to match physiological conditions before a wound occurs. Once severed, boundary conditions to model blood flow may include inlet pressure/flow conditions and an outlet pressure specification (typically atmospheric pressure). At this scale, modeling efforts should include variable resistance to flow (changing vessel diameter) to divert flow away from the site of injury. At the vessel scale (mm), parabolic flow is assumed in the healthy vessel. In the event of trauma, pressure and flow specifications are both possible, which are set by the global hemodynamic model, with the extrinsic coagulation pathway (tissue factor) being the predominant trigger for maintaining hemostasis. Transfusion, vasopressors, and clotting modulators are standard treatment options.

1.2 Global hemodynamics during trauma

Quantifying the regulation of systemic blood pressure has been driven by pharmacology research of hypertension, particularly with respect to sodium balance and renal regulation over the course of hours to days. These hypertension models do not account for blood loss but quantify complex interactions between water intake/urine production, renin-angiotensin-aldosterone system, kidney filtering function, the renal sympathetic nerve activity, and ANP (atrial natrietic peptide) and ADH (vasopressin) (9).

In general, understanding the time-dependent global hemodynamics is essential to predicting hemodynamic collapse and mortality during trauma – and must be accounted for in models of a trauma patient. In cases where trauma and hemorrhage lead to shock, relevant changes can occur on a relatively fast time scale and typically involve: transcapillary water shifts, hypoxia/acidosis, the baroreflex, sympathetic nervous system responses, and the hypothalamic-pituitary-adrenal (HPA) triad (especially during traumatic brain injury).

To some extent, models of blood pressure control have started to account for traumatic bleeding. Hemodynamic models of the systemic circulatory system often employ lumped-parameter methods that implicitly assume uniform distributions of pressure, velocity, and hematocrit within a vascular compartment, resulting in a system of ordinary differential equations (ODEs). They often use an analogy with electrical circuits, where blood flow, viscous dissipation, and pressure drop are analogous to current, resistance, and voltage, respectively. Within this analogy, the frictional losses are modeled by resistors, the inertance of blood flow is captured by inductors (typically only significant in relatively large vessels), and vessel elasticity is represented by capacitors. In circuit analysis, Kirchhoff's current and voltage laws are the primarily tools for determining voltage drops and current flows through every component of the circuit; the former enforces conservation of current and the latter enforces conservation of energy. The early **Otto Frank** 2-component Windkessel model (8) included a capacitor to capture the storage of stressed blood volume in the large arteries in parallel with a resistor to account for the dissipative losses of blood flow through the vasculature, resulting in the following ODE:

$$F(t) = \frac{P(t)}{R} + C\frac{dP(t)}{dt} \tag{4}$$

where F(t) is the flowrate of blood (ml/s), P(t) is the mean arterial pressure (mmHg), C is the arterial compliance(mL/mmHg), and R is the peripheral resistance (mmHg*sec/mL). This model has an exponentially decaying solution:

$$P(t) = P(t_o)e^{\frac{-(t-t_o)}{RC}} \quad (5)$$

which remains useful in medical settings for estimating arterial compliance (10). However, this model does not provide pressure and flow information in each vascular compartment and does not include regulatory responses to blood loss.

The **Guyton-Coleman** model (11), the most famous and extensive model of the circulatory system, contains hundreds of equations and parameters with each vascular compartment characterized by its own compliance, inductance, and resistance depending upon its flow characteristics. The models most salient (and perhaps limiting) feature (12) is the dominant role of the kidney in long-term blood pressure control. The model emphasizes the vital importance of renal control of blood volume in maintaining physiological blood pressures in response to any kind of perturbation (blood loss, salt intake/extraction imbalances, etc.) and quantifying the kidney's response to these changes. The importance of the Sympathetic Nervous System (SNS) to maintain long-term blood pressure control is only marginally captured in the original Guyton-Coleman model (11), and may require extension to include SNS regulation (9).

Particularly relevant to traumatic blood loss, the **Ursino** model includes an elastic variable description of the heart, a parallel arrangement of splanchnic and extrasplanchnic circulations, and neuroregulation via the baroreflex for short-term arterial pressure control (minutes) (7). The baroreflex maintains cardiac output and systemic arterial pressure by regulating systemic resistance, heart period via SNS control, end-systolic elastance, and venous unstressed blood volume. Interestingly, a sensitivity analysis of each of these variables has shown that venous unstressed blood volume is the predominant mechanism for protecting the body from acute blood loss. The model was subsequently extended and able to simulate isocapnic hypoxia and hypercapnia (13–15). While other descriptions of the heart have been proposed and included in other models (16,17), the elastic variable description remains the most widely used because of its physical transparency and straightforward implementation (18,19).

In the **Reisner-Heldt** model (6), a cardiovascular electric circuit model with baroreflex regulation, transcapillary fluid exchange, and lymphatic flow was constructed to model hemorrhage. Parameter values for fluid exchange and lymphatic flow were first tuned with canine blood loss data and then tested against further data sets. To simulate hemorrhage, a resistor was connected to atmospheric pressure and tuned to match blood volume loss as a function of time; once set, the resistance was held constant for the remainder of the simulation. The model predicted that in the initial stages of moderate to severe hemorrhage,

transcapillary fluid exchange was significant in limiting hypovolemia and antagonistic to protein return. In the dehydrated patient, hydrostatic pressure in the interstitial tissue was too small to return protein to the vasculature after blood loss and the model predicts an increased risk of hemodynamic collapse.

The **Neal-Bassingthwaighte** (20) model was the first one with the capability of making trauma episode-specific predictions. The model used the electrical circuit analogy to construct a closed-loop circulation system with baroreceptor regulation. Parameters were determined by tuning the model to match baseline physiology of pigs prior to injury to the heart wall, and then held constant post-injury in the open-loop format. Rather than assuming a hemorrhage rate at a specific location (as in the **Reisner-Heldt** model), the tuned parameters were used in combination with arterial blood pressure and heart rate measurements (used as inputs to the model) to estimate cardiac output and total blood volume, which were validated via flowprobe measurements and survival/death outcomes of the pigs. Since the model did not explicitly account for diminished sympathetic vasoconstriction or cardiac contractility near the point of death, cardiac output measurements at those points were the most difficult to predict accurately.

The **Sterling-Summers** model extended the Guyton Model to explore the effects of morbid obesity on Mean Arterial Pressure (MAP) and Cardiac Output (CO) during hemorrhage (21). Body mass Index (BMI) was used to quantify obesity, parameter values were tuned

from known population distributions, and percent changes in hemodynamic quantities were calculated and compared with non-obese patients. Interestingly, the model predicts significant decreases in MAP and CO in response to modest increases in BMI. A systems analysis of the virtual obese patient revealed that an increase in the resistance to venous return that results from increased intra-abdominal pressure is responsible for this. This implies that a greater quantity of fluid during resuscitation is essential to overcoming the resistance to venous return in the obese patient. Since the model is constructed with mean values from population distributions, it is unable to make real-time patient-specific prediction.

The **Mazzoni-Skalak** microcirculatory network model was based upon the rat spinotrapezius muscle and considered 389 microvessels originating from a single arteriolar tree and converging to a single collecting venule while tracking the flow of leukocytes through the network (21). Resistance parameter values were calculated by assuming Poiseuille flow through the microvasculature (correcting for viscosity changes using empirical relationships that relate viscosity to diameter, hematocrit, and shear rate) so that flowrate could be calculated in response to an applied pressure. Once a leukocyte attempted to enter a vessel smaller than its diameter, it would deform and increase the resistance to capillary flow. The simulation was used to study the relative importance of mechanisms responsible for slow reperfusion following ischemia and predict blood flowrates and composition in response to measurable changes in pressure, hematocrit, and capillary diameter in the left gastrocnemius muscle of bleeding anesthetized rabbit. Interestingly, the

model also predicted that the slow reperfusion that characterizes ischemia is intensified if the leukocytes become active during ischemia.

The **Hirshberg-Mattox** model incorporated hemodilution into a hemodynamic model to evaluate the transfusion guidelines preventing dilutional coagulopathy in a bleeding patient (22). Hirshberg et al. argued that plasma and platelet replacement were based upon empirical guidelines derived from a simple mathematical model with assumptions that frequently do not hold in severe trauma patients. For example, the model assumed a stable blood volume and that replacement rate is constant and equal to blood loss rate - in reality, blood loss is a function of blood pressure (not a constant), and replacement follows blood loss (sometimes on the order of many minutes or hours). Furthermore, the original model was derived when whole blood transfusion was the standard protocol – not the packed red blood cell (PRBC) transfusions used today – thus underestimating required concentrations of clotting factors. The model accounted for the heterogeneity of blood by explicitly including red blood cells, plasma, and intravascular water. The circulation system was described with the same nonlinear function relating systolic pressure to blood volume developed by Lewis (23). Interestingly, the model was able to predict that resuscitation with more than 5 units of RBC will unavoidably lead to dilutional coagulopathy, and that the optimal ratio of fresh frozen plasma (FFP) to PRBC is 2:3, with an initial 2:1 ratio being essential to preventing dilutional coagulopathy.

1.3 Modeling of tissue scale bleeding

Defining vascular networks in silico. In solving for the flow through a tissue that has been damaged, the hemodynamics of a branching vascular network becomes relevant. Vascular network modeling has been well-studied by numerous researchers. The earliest theoretical analysis for the design of the vasculature network was Murray's "minimum dissipation principle", which stated that the parent-vessel bifurcation occurs in such a way as to optimize the balance between the operational costs that arise from viscous energy losses (decreases with increasing diameter) and the capital cost of large blood vessels and large blood volume (increases with increasing diameter) (2). The most significant equation that arises from this analysis is a rule that governs how the parent vessel bifurcates into daughter vessels:

$$d_0^{\gamma} = d_1^{\gamma} + d_2^{\gamma}$$

Where d_0 is the diameter of the parent vessel, d_1 and d_2 are the diameters of the daughter vessels, and γ is the branching exponent. In Murray's law γ is set to 3, although other researchers have found that values between 2 and 3 are also physiological in certain vascular beds (24,25). Other parent-daughter relations for bifurcating network relations are possible for generating realistic vascular tree networks. A constant parent-daughter ratio specification (26) can match measured geometries, as can stochastic sampling of branch/generation distributions. The bifurcation angles are then typically defined, although there is large variability in the angles depending upon the location and target (27). Realistic

vascular networks have been created in silico with these rules in other studies (28–30), although not in the context of traumatic bleeding. The **Westerhof** model depicted the systemic arterial tree as an electrical circuit to model the viscoelastic properties of the arterial wall, but this representation is less common (31).

Defining regulatory mechanisms in bleeding tissue

In deploying network models for bleeding by a tissue, a branching network progresses from a large feeding artery to arterioles to capillaries and then de-branches to venules and larger collecting veins. Severing an arteriole or a vein, for example, results in distinct flow changes upstream and downstream of the injury. Arterial injury is characterized by high pressures driving blood loss and disrupted perfusion of all distal vessels. Venous injury is characterized by bleeding driven at lower pressures, with less likely immediate impact on the upstream arterial perfusion of the tissue.

In arterial injuries, the blood vessel's high pressure is suddenly exposed to atmospheric pressure and bleeding rate becomes a function of pressure difference, oxygen consumption, cardiac output, and resistance to flow towards the exit. In the limit of complete severing of the vascular network, local downstream resistance is entirely lost, further increasing blood loss from the wound. In the event of internal bleeding, which is common following trauma, bruising can often be observed due to blood pooling in the body. In venous injuries, additional complications arise when considering the compliance of the veins -- large vein

resistance varies depending upon how compressed they are by their surroundings, or distended due to the flow of blood. However, during trauma, high venous compliance and small filling pressure can lead to venous collapse. This phenomenon was indirectly addressed in Ursino's model, where an exponential function was used to describe the relationship between pressure and volume in the veins (7). The body's immediate response to this perturbation in blood volume is the response of the baroreflex, which attempts to maintain cardiac output by regulating venous blood volume, systemic resistance, and heart rate. Vessel diameters are also varied to divert blood flow away from the site of injury and minimize blood loss. On a larger time-scale (minutes to hours), transcapillary fluid exchange in a well-hydrated patient occurs to diminish, to a limited extent, the effect of hypovolemia (6).

Efforts to model bleeding networks requires inlet/outlet pressure or flow boundary conditions (as functions of time), conservation of flow restrictions at branching points, and regulatory mechanisms to account for the action of the baroreflex and the fluid shifts. Researchers have applied inlet pressure/flow boundary conditions and local vasoregulation effectively to model this phenomenon in the construction of the cardiovascular system and vascular networks (27,32). In the context of traumatic bleeding, the most natural outlet boundary condition would be a pressure specification since it is held constant at P_{atm}, although a bleeding rate specification may also be possible. The downstream condition for intact cardiovascular system post-injury could also be pressure/flow specifications,

although 3-element windkessel boundary conditions (33) and wave reflection coefficient specifications have also been used (34).

Formaggia et al. developed a multiscale model of the circulatory system by coupling a zero-dimensional, lumped parameter model with a carotid bifurcating model (31). The lumped parameter model provided pressure boundary conditions to the bifurcating model, while the bifurcation model provided flowrates to the global hemodynamic model. Although not used to study traumatic bleeding, a variation of this coupling strategy will be helpful in developing a full multiscale model of a trauma patient (35,36).

1.4 The hemostatic response in traumatized vessels

In daily life, the routine hemostatic response to vessel injury is well regulated. Platelets are captured by the injured wall and activate to release ADP and synthesize thromboxane (TXA_2) to drive further platelet deposition. The buildup of a platelet mass is highly hemostatic. Additionally, the extrinsic coagulation pathway is initiated when the cofactor Tissue Factor (TF) is exposed to blood near the site of injury and binds Factors VII and VIIa. The TF/FVIIa complex (sometimes called the extrinsic tenase) generates FXa and FXIa (37). Generation of the intrinsic tenase complex FIXa/FVIIIa results in a burst of FXa, resulting in prothombinase (FXa/FVa) to help drive the generation of thrombin (FIIa). Thrombin is essential for platelet activation and for fibrin polymerization to stabilize the clot structure. Because FXIIa or FXIa deficiency is not associated with hemophilia, the contact pathway is considered nonessential for hemostasis. However, the requirements for

hemostasis are substantially more challenging during trauma. Since contact pathway deficiency is associated with some risk for surgical bleeding, TIC risks may exist in trauma patients lacking FXII and FXI. The role of FXII and FXI in traumatic bleeding is not well studied.

From a systems biology perspective, the kinetics modeling of isotropic coagulation protease cascade has progressed over several decades and has been extensively reviewed (38–42). These models mostly focus on the rate of thrombin generation and the clotting time when a threshold level of thrombin has been reached, although some have progressed towards trauma in silico (43).

Modeling of blood clotting under non-flow conditions. One of the oldest ODE (lumped) models of coagulation is the **Hockin-Mann** model (44), which utilized 34 ODEs and 42 kinetic parameters to describe the extrinsic pathway. This model predicted coagulation initiation as [TF] was increased from 1 to 25 pM (zero clotting if TF is absent). A sensitivity analysis performed by Danforth et al. (45) indicated that the model was highly sensitive to parameter choice characterizing FVIIa with TF interactions. Model limitations include implicit assumption of an activated and excess platelet surface for coagulation to begin and did not include the contact pathway, and therefore, could not predict blood clotting in the absence of TF.

The **Chatterjee-Diamond** "platelet-plasma" ODE model (46) extended the Hockin-Mann model to 76 ODE's and 105 kinetic parameters to include the extrinsic pathway and characterize the initiation of coagulation in the absence of TF. It also included thrombin and contact mediated feedback of FXIa generation and was able to predict FXIIa generation in the presence of CTI (corn trypsin inhibitor), a feature that was confirmed experimentally. The model included the role of platelet activation to reduce the initiation time for coagulation. Like the Hockin-Mann model, the platelet-plasma model assumes excess platelet surfaces. Recent experiments under flow indicate that the first layer of depositing platelets is sufficient for most of the thrombin produced on a TF bearing surface (47), confirming that platelets are not likely rate-limiting, at least at healthy platelet levels.

Bungay-Gentry model developed an isotropic reaction network model (48) with 73 ODEs and 17 reversible lipid adsorption reactions to explicitly account for lipid binding. While the reaction mechanisms were quite different from the Hockin-Mann model, they both agree with the same experimental study (49). Their model predicts a threshold value of 25 nM lipid required for thrombin generation with 30-200 nM lipid range being most ideal.

Platelet Models. Modeling of platelet signaling during clotting often use simple models of platelet activation typically with activation states of platelets as binary, either resting or fully activated depending upon an "activator concentration", which can be a lumped

representation of several species. This approach often is not tested against data sets with individual signaling pathways modulated pharmacologically.

Toward a detailed description of receptor-mediated platelet activation, the **Purvis-Diamond** model (50) used 77 reactions and 132 parameters to describe ADP-mediated signaling of P2Y1 G-coupled protein receptor activation, phospholipase-Cb activation, protein kinase C activation, phospohoinositol metabolism, and IP3 receptor regulation. The model was able to predict Ca_{2+} levels and ADP dose-responses, phosphoinositide metabolism, and volume of the dense tubular system. This ODE representation of the activation state of a platelet can then be included as a submodel of a larger-scale modeling of platelet aggregation. An ODE reaction network around platelet store-operated calcium entry (Stim1/Orai) predicts calcium mobilization in the presence of extracellular calcium. Lenoci and Hamm (51) used a system of ODE's to describe kinetics of PAR-1 activation to generate intracellular signals that lead to platelet aggregation.

While these ODE models for P2Y1 and PAR1 signaling are full descriptions, they prove unwieldy in hemostatic clotting with single cell resolution and are difficult to tune to an individual patient. Chatterjee used a high throughput assay to measure [Ca2+] responses to 18 single agonist stimulations (6 agonists * 3 doses) and to 135 pairwise combinations of the agonists, an experimental technique termed pairwise agonist scanning (PAS). The data was used to train a neural network model (52) to make patient-specific platelet intracellular

Ca^{2+} predictions in response to pairwise combinations of 6 agonists and to stimulate P2Y1/P2Y12, TP, IP, PAR1/4, GPVI membrane receptors, as well as intracellular guanylate cyclase. This later became an instrumental tool in multi-scale simulations of thrombosis under flow.

Clotting with flow. The **Kuharsky-Fogelson** model (53) used 59 ODE's to describe blood clotting on a Tissue Factor (TF) surface, simultaneously accounting for blood flow and platelet function. The model described blood flow over a TF patch that was small enough to make spatial variations in concentration negligible, enabling an ODE representation. The model was later extended to a PDE formulation (54) to account for concentration gradients in the growing thrombus. The model treated platelets as chemical solutes, and lumped mass-transfer coefficients were used to characterize transport of co-factors, enzymes, platelets, and inhibitors to the injured surface. The model predicted a thrombin generation threshold dependence on surface [TF] that was consistent with experimental results (55). The PDE formulation of the model was used to calculate concentration variations within the thrombus, with the changing velocity field characterized by solution of the Navier-Stokes equation undergoing Brinkman flow. The model predicted that the thrombus was strongly dependent upon wall shear rate and physical blocking of TF, the latter being a strong inhibitor of coagulation. The model also predicted the classic thrombus architecture of an inner core of fully activated platelets, and an outer shell of less-activated platelets (56). Importantly, this is a model of clotting on a

surface and does not consider boundary conditions associated with bleeding hemodynamics.

Xu et al. used interacting submodels to develop a multiscale simulation of thrombus growth (57). A coagulation cascade was coupled with a stochastic cellular Potts model of platelet states (motion, adhesion, deformations from the flow, activation state, etc.). Additionally, the **Filipovic-Tsuda** model used dissipative particle dynamics (DPD) to model thrombosis (58). The model explicitly accounts for platelet motion and interactions with other platelets and the vessel wall. By integrating the DPD equations in time, the model was able to simulate thrombotic events in small stenotic flow channels while explicitly tracking the behavior of each individual platelet over time. Again, these thrombosis models do not consider the boundary conditions of bleeding and hemostasis.

1.5 Machine learning in trauma

The **Flamm-Diamond** model used a patient-specific NN model (39) as one of four interacting submodules of a multi-scale simulation of thrombosis under flow. The model required simultaneous solution of the velocity field in the presence of a growing clot via the Lattice Boltzmann method, solution to the convection-diffusion-reaction equation via the Finite Element Method (FEM) for the concentration profiles of ADP and TXA_2, platelet activation states in response to concentrations of soluble agonists from the NN, and platelet motion and binding via the Lattice Kinetic Monte Carlo (LKMC) method. A platelet drift velocity and an inlet platelet concentration distribution biased to be larger near the walls were included to account for red blood cell motion. The NN was able to provide patient-

specific platelet information making it a highly valuable tool for predicting blood clotting under flow, as well as predicting the ranked potency of several drugs. This represented the first instance of patient-specific predictions of platelet deposition under flow and may have consequences in determining responses to therapy in the future. This model was extended (**Lu-Diamond** model) to include thrombin-dependent platelet signaling during clot buildup in the presence of various pharmacological inhibitors (59). While no models yet calculate intrathrombus fibrin generation and fibrins anti-thrombin-1 activity, the Lu-Diamond model imposed a biphasic wall flux of thrombin that recapitulates the massive inhibitory action of fibrin against thrombin. Recent measurements prove that most thrombin is captured by intrathrombic fibrin [67].

Current limitations in various clotting models include the difficulty of 3D simulation, lack of pulsatile flow conditions, and difficulty of solving problems on a full arterial length scale. Also for multicomponent reaction systems, different sets of reaction networks and parameterizations may equally fit the data [57], making validation difficult. To date, few mathematical models have been tested for clots growing under diverse flow, biochemical, and pharmacological conditions. Through course graining with an imposed thrombin generation rate at a tissue factor surface, Lu et al. was able to simulate clotting under flow for several relevant pharmacological conditions. However, a full simulation of thrombin generation, platelet activation, and fibrin polymerization has not yet been validated for healthy blood or for trauma blood. Additionally, clotting models have not been tested for boundary conditions of bleeding where clot strength is an important emergent property.

Also, flow-clotting models have not yet been parameterized for trauma blood, where platelets are so highly dysfunctional [33].

CHAPTER 2 Coagulopathy Implications using a multiscale model of traumatic bleeding matching macro and microcirculation

2.1 Abstract

Quantifying the relationship between vascular injury and the dynamic bleeding rate requires a multiscale model that accounts for changing and coupled hemodynamics between the global and microvascular levels. A lumped, global hemodynamic model of the human cardiovascular system with baroreflex control was coupled to a local 24-level bifurcating vascular network that spanned diameters from the muscular artery scale (0.1 – 1.3 mm) to capillaries (5-10 μm) via conservation of momentum and conservation of mass boundary conditions. For defined injuries of severing all vessels at each n^{th}-level, the changing pressures and flowrates were calculated using prescribed shear-dependent hemostatic clot growth rates (normal or coagulopathic). Key results were: (1) the upstream vascular network rapidly depressurizes to reduce blood loss, (2) wall shear rates at the hemorrhaging wound exit are sufficiently high (~10,000 s^{-1}) to drive von Willebrand Factor unfolding, (3) full coagulopathy results in >2L blood loss in 2 hours for severing all vessels of 0.13 to 0.005 mm diameter within the bifurcating network, whereas full hemostasis limits blood loss to <100 mL within 2 min, and (4) hemodilution from transcapillary refill increases blood loss and could be implicated in trauma induced coagulopathy. A sensitivity analysis on length/diameter ratio and branching exponent demonstrated that bleeding was strongly dependent upon these tissue-dependent network parameters. This is the first bleeding model that prescribes the geometry of the injury in order to calculate the rate of

pressure-driven blood loss and local wall shear rate in the presence or absence of coagulopathic blood.

2.2 Introduction

Uncontrolled bleeding is the third leading cause of mortality in the US and is the leading cause of death in those 35 years of age and younger (60). Predicting patient bleeding trajectories (rate of bleeding and rate of hemostasis) following injury may help identify patients at risk for trauma-induced coagulopathy (TIC) or guide transfusion decisions (61–64). However, traumatic bleeding is intrinsically multiscale and heterogeneous in both space and time. Tissue trauma simultaneously drives microscopic cellular responses via biochemical reaction networks operating at sub-second timescales, while also being modulated by patient-scale processes (e.g., baroreflex) occurring over minutes and hours. Consequently, a computational model can help relate the evolution of global hemodynamic quantities such as blood pressure, heart rate, and total blood volume with local injury site properties such as local blood flow and bleeding rates, wall shear rates, local pressure gradients, and clotting dynamics.

Models of the cardiovascular system may be broadly classified into three categories according to their spatial resolution. At the patient scale are global hemodynamic (GH) models that describe the overall state of the patient in terms of quantities such as heart rate, blood pressure, and total blood volume. GH models usually represent a patient by a series of interconnected 0-dimensional (lumped) compartments, each of which is characterized

by a flow resistance and capacitance (11,65–67). GH models may include descriptions of various phenomena (e.g., baroreflex (67,68)) and disease states (e.g., hypertension (66)). Next, branching vasculature network (BVN) models are used to describe blood flow through continuously bifurcating blood vessels from the arterial to the capillary scale (~mm - μm) (27,69). Here, bifurcating networks are defined by an initial root vessel diameter, a length-to-diameter (L/D) relationship, and rules for vessel bifurcation (i.e., branching angle and vessel diameter). Such networks have been used primarily for investigating flow heterogeneity, oxygen transport, and understanding how disruptions in the vessel network architecture are implicated in disease. Finally, single-vessel (SV) models (~μm) have been constructed to model clotting under flow in response to collagen and tissue factor surface (54,57,59). These models typically employ interacting submodules for solving for concentration gradients of agonists involved in clotting, flow fields in the presence of a growing clot, and platelet motion.

To date, mathematical models of hemorrhage generally have relied on GH formalisms coupled with a prescribed bleeding rate (20,22,70,71). The Reisner-Heldt model simulated hemorrhage by connecting a resistive pathway to atmospheric pressure and tuning the resistance to match blood volume loss to experimental data (70). The Neal-Bassingthwaighte model used live arterial blood pressure and heart rate measurements from bleeding pigs to make predictions about total blood volume and cardiovascular output within the pig (20). The Ursino model was used to study the effects of a 10% blood volume reduction over a 5 second interval on various bodily responses (67). However, a more

predictive framework for bleeding requires explicit connections between bleed rates and damage to individual blood vessels. Recently, Canuto et al. coupled a GH model of the cardiovascular system with a 1-dimensional representation of large systemic arteries to study trauma by exposing a severed blood vessel to atmospheric pressure and modeling tourniquet application to the damaged region (68). Our model couples a GH model to a damaged BVN to quantify the response to bleeding in the absence of external intervention and in the presence/absence of factors such as vasoconstriction, high shear rate clotting, and hemodilution.

Here, we present a multiscale model of a trauma patient that spans 6 orders of magnitude, from the patient scale (m) to the single vessel scale (μm). The model couples a global hemodynamic module with a bifurcating vascular network model containing 24 generations of vessel diameters for a total of 33,554,431 vessels. Wound states are specified by deleting a portion of the vessel network and imposing atmospheric pressure conditions at the wound site. Hemostasis is modeled according to a prescribed shear-dependent, transient sealing rate function that is based on direct measurements of healthy blood clotting under flow (72). External interventions such as tamponade were not included as we aimed to observe the bodily response to trauma. Using this modeling framework, we study bleeding dynamics due to wounds at different vessel scales, with and without hemostasis. We also demonstrate, for the first time, the importance of local depressurization near wound sites on predicted bleeding rates. Additionally, the simulations predicted pathologically high wall shear rates on the order of 10^4 which have

been demonstrated to elongate and multimerize von Willebrand Factor (VWF) into thick fibers (73,74). These calculations, which include baroreflex, vasoconstriction, and hemodilution, support the contention that wall shear rates are extremely high during traumatic bleeding.

2.3 Model Description

2.3.1 Global Hemodynamic Model (GH)

The global hemodynamic module employed in this study is a variation of the Ursino model (14,67,75), which consists of multiple, interacting 0-dimensional (lumped) arterial and venous compartments (Fig. 2-1). The compartments are arranged in a combination of series and parallel configurations and coupled to an elastic pulsatile description of the heart and a baroreflex control loop to model the cardiovascular system. The model enforces conservation of mass within each compartment so that

$$\boxed{\frac{dP_i}{dt} = \frac{1}{C_i} * (F_{in} - F_i),} \quad (1)$$

where P_i, C_i, and F_i are, respectively, the pressure, capacitance, and flowrate through the i^{th} compartment and F_{in} is the incoming blood flow rate. Equation 1 applies to each of the following compartments shown in Fig. 2-1: pulmonary arteries (*pa*), pulmonary peripheral (*pp*), pulmonary veins (*pv*), systemic arteries (*sa*), systemic peripheral (*sp*), splanchnic veins (*sv*), skeletal muscle veins (*mv*), brain veins (*bv*), and coronary veins (h*v*). For the large *sa* and *pa* compartments, an additional force balance is imposed to account for blood acceleration, i.e.,

$$\frac{dF_i}{dt} = \frac{1}{L_i} * (P_i - P_j - R_i F_i), \quad (2)$$

where L_i and R_i are the inertance and resistance of the compartment, respectively, and P_j is the pressure of the downstream compartment.

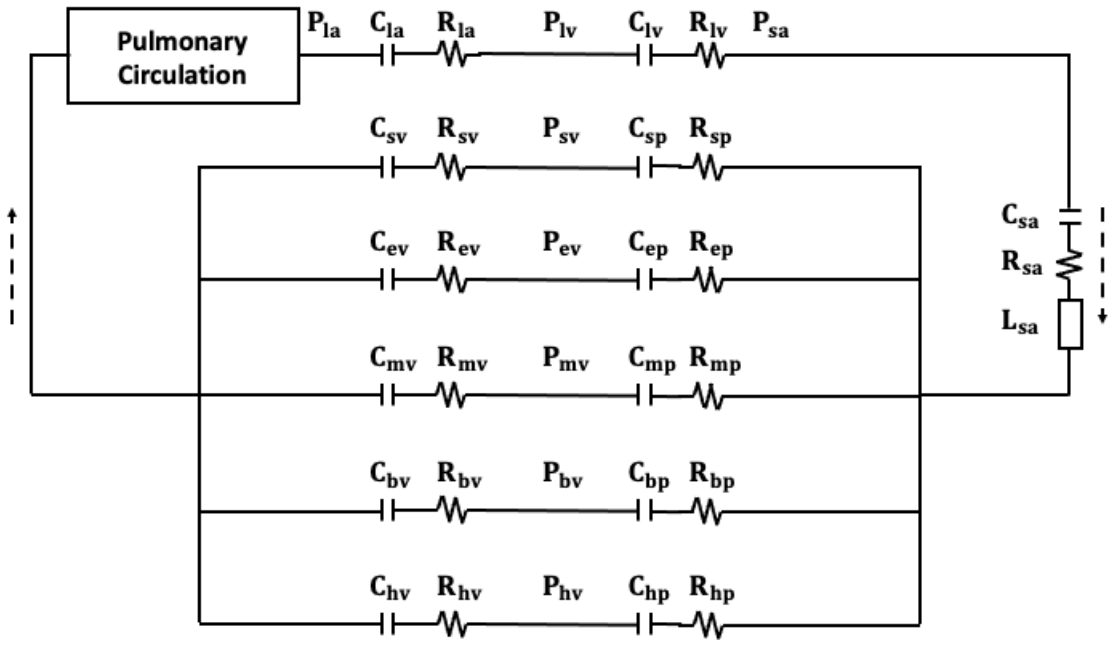

Fig. 2-1 Global hemodynamic model. Closed-loop flow diagram of the global hemodynamic (GH) model in the absence of bleeding. The patient is represented by interconnected, lumped, compartments, composed of resistances, capacitances, and - in large arteries - inertances. P: Pressure, C: Capacitance, R: Resistance, L: Inductance, la: left atrium, lv : left ventricle, sp: splanchnic peripheral, sv: splanchnic venous, ep: extrasplanchnic peripheral, ev: extrasplanchnic venous, bp: brain peripheral, bv: brain venous, hp: heart peripheral, hv: heart venous. mp: muscle peripheral, mv: muscle venous.

The extrasplanchnic venous (*ev*) pressure is automatically constrained by the total blood volume to guarantee conservation of mass in the circulatory system, i.e.,

$$P_{ev} = \frac{1}{C_{ev}} * \left(V_{tot} - \sum_i (C_i P_i) - V_{rv} - V_{lv} - V_u \right), \quad (3)$$

where V_{tot} is the total blood volume, V_{rv} and V_{lv} are the volumes of the right and left ventricles respectively, and V_u is the total unstressed blood volume in the body. V_u is computed as the sum of the unstressed blood volume in the individual compartments,

$$V_u = \sum_i V_{u,i}, \quad (4)$$

where the summation includes the *sa*, *sp*, *sv*, *ev*, *mv*, *bv*, *hv*, *pa*, *pp*, *pv*, extrasplanchnic peripheral (*ep*), muscular peripheral (*mp*), brain peripheral (*bp*), heart peripheral (*hp*), right atrium (*ra*), and left atrium (*la*). For all simulations presented in this study, the total blood volume was initialized to 5.3L, which corresponds approximately to the blood volume of a 80kg male (76).

The driving force of the global hemodynamic model is given by the pressure-volume relationship of the left-heart

$$P_{lv} = \varphi(t) * E_{max,lv} * (V_{lv} - V_{u,lv}) + (1 - \varphi(t)) * P_{0,lv} * (e^{K_{E,lv} * V_{lv}} - 1) - R_{lv} F_{o,l} \quad (5)$$

Where $E_{max,lv}$ is the elastance of the left ventricle, $V_{u,lv}$ is the unstressed volume of the left ventricle, $P_{0,lv}$ and $K_{E,lv}$ are coefficients that govern the exponential pressure decay at diastole, R_{lv} is the resistance to flow in the left ventricle, and $F_{o,l}$ is the cardiac output from the left ventricle. The first term assumes a linear relationship between left-ventricle pressure at end systolic volume, while the second term assumes an exponentially decaying relationship at diastole. The function φ(t) describes ventricle activation and is given by,

$$\varphi(t) = \begin{cases} sin^2 \left[\dfrac{\pi * T(t) * u}{T_{sys}(t)} \right] & , \ 0 \leq u \leq \dfrac{T_{sys}}{T} \\ 0 & , \ \dfrac{T_{sys}}{T} \leq u \leq 1 \end{cases} \quad (6)$$

where u is a dimensionless variable representing the fraction of the cardiac cycle, T_{sys} is the duration of systole, and T is the heart period. Equations (5) and (6) govern the pressure and pulsatile nature of the heart. An analogous set of equations was used to simulate the pulmonary circulatory system.

The arterial baroreflex is modeled by a set of 11 equations controlling vagal and sympathetic stimulation in the body (see Ref. (14,67,75)). The following properties are impacted by the baroreflex response: ventricle elastances, unstressed blood volumes, and peripheral resistances. Each property, θ, is updated temporally according to

$$\theta(t) = \Delta\theta(t) + \theta_0, \tag{7}$$

where $\Delta\theta(t)$ is the change in the property over a specified time interval due to baroreflex control, and θ_0 is the basal value. The heart period also is impacted by the baroreflex response,

$$T = (\Delta T_s + \Delta T_v) + T_0, \tag{8}$$

where ΔT_s represents sympathetic stimulation influence on the heart period, ΔT_v is the vagal stimulation influence on heart period, and T_0 is the basal heart period.

2.3.2 Branching Vasculature Network Model (BVN)

We adopt the branching vasculature network model of Yang et al. (27), which specifies an initial arterial root diameter, a length-to-diameter ratio for all vessels, and assumes a power law relationship that governs how the parent vessel bifurcates into two daughter vessels, i.e.,

$$d_0^k = d_1^k + d_2^k, \tag{9}$$

where d_0 is the diameter of the parent vessel, d_1 and d_2 are the diameters of the daughter vessels, and k is the branching exponent. This bifurcation relationship has been well-studied and extensively reviewed, with $k = 3$ frequently referred to as Murray's "minimum dissipation principle" in 2 dimensions (77). Bifurcation angles were determined based upon the total volume minimization principle of Murray (77), i.e.,

$$\cos(\theta_1) = \frac{d_0^4 + d_1^4 - d_2^4}{(2d_0d_1)^2}, \cos(\theta_2) = \frac{d_0^4 - d_1^4 + d_2^4}{(2d_0d_1)^2}. \tag{10}$$

In the present study we assume that the two daughter vessels have the same diameter, i.e., $\theta_1 = \theta_2$ at all vessel sizes. Yang et al. generated a 3-dimensional vessel network by introducing a rotation at each generation. In ref. (27), rotation angles at each generation were determined by optimizing an objective function that balances space filling,

gravitational, and centripetal forces. Here, we assume a fixed 60° rotation angle for simplicity (Panel A, Fig. 2-2). Note that the choice of rotation angle only affects the vessel-to-tissue volume ratio and does not impact the hemodynamic results.

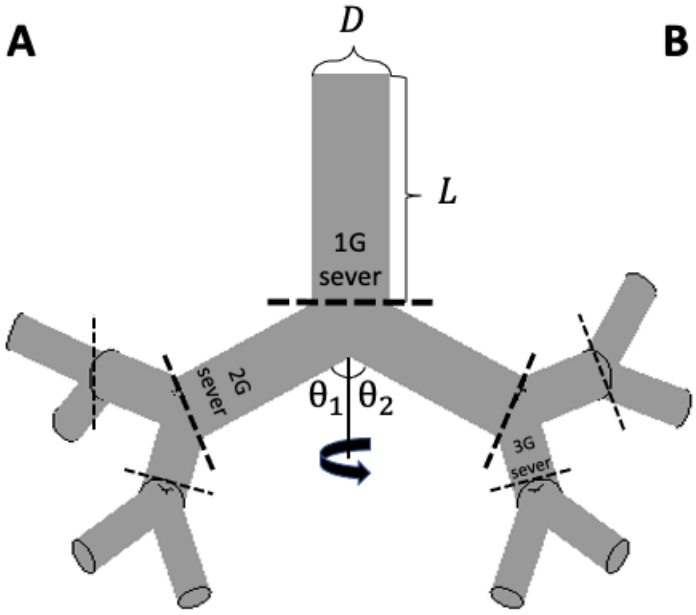

B

Generations	Diameter (mm)	Flowrate (mL/s)
0	1.30×10^{0}	1.46×10^{-1}
1	1.03×10^{0}	7.31×10^{-2}
2	8.19×10^{-1}	3.65×10^{-2}
3	6.50×10^{-1}	1.83×10^{-2}
4	5.16×10^{-1}	9.13×10^{-3}
5	4.09×10^{-1}	4.57×10^{-3}
6	3.25×10^{-1}	2.28×10^{-3}
7	2.58×10^{-1}	1.14×10^{-3}
8	2.05×10^{-1}	5.71×10^{-4}
9	1.63×10^{-1}	2.85×10^{-4}
10	1.29×10^{-1}	1.43×10^{-4}
11	1.02×10^{-1}	7.14×10^{-5}
12	8.13×10^{-2}	3.57×10^{-5}
13	6.45×10^{-2}	1.78×10^{-5}
14	5.12×10^{-2}	8.92×10^{-6}
15	4.06×10^{-2}	4.46×10^{-6}
16	3.22×10^{-2}	2.23×10^{-6}
17	2.56×10^{-2}	1.12×10^{-6}
18	2.03×10^{-2}	5.58×10^{-7}
19	1.61×10^{-2}	2.79×10^{-7}
20	1.28×10^{-2}	1.39×10^{-7}
21	1.02×10^{-2}	6.97×10^{-8}
22	8.06×10^{-3}	3.48×10^{-8}
23	6.40×10^{-3}	1.74×10^{-8}
24	5.08×10^{-3}	8.71×10^{-9}

Fig. 2-2 Bifurcated vasculature network and pressure matching. A schematic of a 3-generation branching vasculature network (BVN) is shown (A) along with examples of a first generation (1G), second generation (2G), and third generation (3G) vessel sever. The diameter (D), length (L), and the angles between each of the blood vessels within the same plane (θ), are provided for clarity. Traced lines show where severs to the network take place when referring to either a 1G, 2G, or 3G sever. Vessel diameters and flowrates of a 24-generation symmetric branching network (no bleeding) are shown in the Table (B). Generations 0-11 represent small arteries, 12-21 represent arterioles, and 22-24 represent capillaries.

To solve for the flow distribution in the BVN, The Poiseuille flow equation was augmented with a bifurcation correction term to account for the additional viscous dissipation associated with a bifurcation in all blood vessels with a diameter <60μm (78). Yang et al. used 3D flow simulations to show that this additional flow resistance arises as an additional parameter in the Poiseuille flow equation:

$$Q = \frac{\Delta P(1-\lambda)}{(\frac{128\mu L}{\pi d^4})}, \quad (11)$$

where ΔP is the pressure drop, μ is the local viscosity, L is the length of the vessel, d is the diameter, and λ is the correction due to bifurcation. The correction term is independent of the size of the angle of bifurcation, suggesting that the act of separating the flow into two distinct parabolic flow streams is what provides the additional resistance to flow (78). The standard Poiseuille flow equation was used to describe terminating vessels. The blood viscosity is estimated by assuming a constant hematocrit of 45% and accounting for the apparent vessel diameter-dependent viscosity (Fahraeus-Lindqvist effect) with the Pries et al. measurements (79),

$$\mu(d) = \mu_0 \left(1 + (\eta(d) - 1)\left(\frac{d}{d-1.1}\right)^2\right) * \left(\frac{d}{d-1.1}\right)^2, \quad (12)$$

where

$$\eta(d) = 3.2 + 6e^{-0.085*d} - 2.44e^{-0.06d^{0.645}}. \quad (13)$$

By enforcing conservation of mass and momentum at the bifurcation points, prescribing pressure boundary conditions at terminal points, and recognizing that the inlet pressure condition to every node of the same generation must be equal for a symmetric vascular network, it is possible to compute the pressure and flow distribution through the entire network.

2.3.3 Multiscale Coupling Strategy

In the following discussion, the muscular peripheral (*mp*) compartment is used to demonstrate the multiscale coupling strategy, although it may be equivalently applied to any compartment. The principal notion of our strategy is to divide a GH compartment into explicit and implicit sub-compartments. Here, the explicit sub-compartment is represented by a BVN that resolves a portion of the blood vessel network in the compartment, while the implicit sub-compartment accounts for the remainder. Moreover, the BVN may be further subdivided into intact and wounded portions, the latter representing a traumatic injury.

As shown in Fig. 2-3, the overall resistance of the compartment may be expressed as a combination of four distinct resistances. The resistance R' corresponds to the (implicit) portion of the compartment comprised of vessels larger than those represented by the BVN. The exit pressure leaving this subcompartment is P* (see below). The subcompartment

corresponding to the resistor R'' represents vessels that are of equal size to those in the BVN but that are not explicitly resolved. The inlet and outlet pressures for this sub-compartment, which is parallel to the BVN, are P_* and P_{out}, respectively. The BVN itself is subdivided into two portions—the first consists of all intact vessels with outlet pressure P_{out} and the second consists of all severed vessels with outlet pressure P_{atm}, i.e., neglecting any interstitial resistance. The two portions of the BVN are characterized by resistances, R_{BVN} and R_w, respectively.

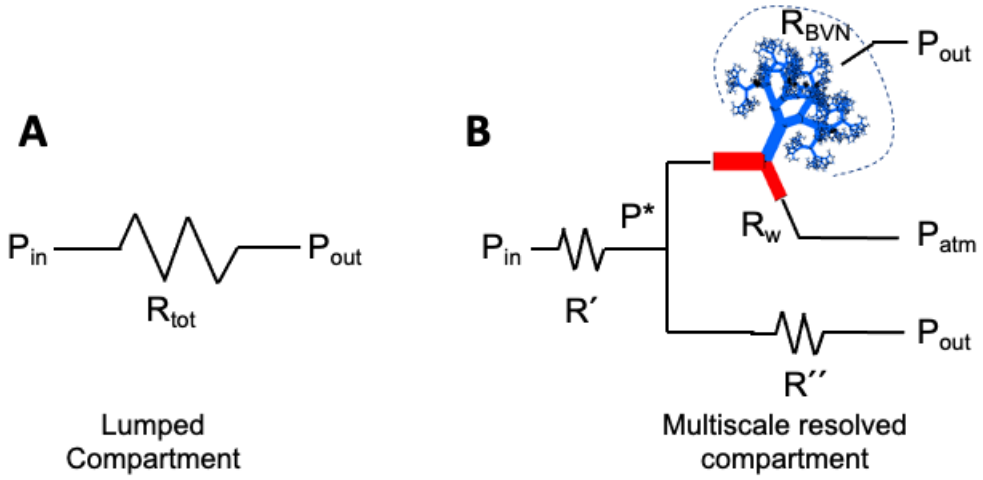

Fig. 2-3 Multiscale coupling strategy *for boundary condition matching where the lumped compartment, macroscale description of resistance (Ursino model) (A) was fully-resolved for traumatic bleeding in parallel with an intact tissue (B). The total resistance value R_{tot} from the Ursino Model is divided into a four-resistance subsystem (R', R'', R_w, R_{BVN}). R' represents the implicit portion of the compartment and is comprised of vessels larger than the branching vasculature network (BVN). R'' represent vessels that are of equal size to those of the BVN but were not explicitly resolved. R_w is the resistance to bleeding, effectively infinite in the absence of bleeding but finite in the presence of bleeding. R_{BVN} is the overall resistance of the BVN computed based on fully-developed, steady state Poiseuille flow with the correction term included (equation (11)) for all relevant blood vessels. The inlet and outlet pressure boundary conditions for intact*

vasculature (no bleeding) were set to P_{in} = 70 mmHg and P_{out} = 25 mmHg. In simulations of bleeding, the outlet pressure was set to P_{atm} = 0 for exposure to the atmosphere.

In the absence of bleeding, i.e., when there are no severed vessels, R_w is effectively infinite, and all blood flow is directed to intact vessels. The relationship between the resistances R', R'', and R_{BVN} is shown in panel B of Fig. 2-3, i.e.,

$$R_{tot} = R' + \frac{1}{\frac{1}{R''} + \frac{1}{R_{BVN}}}. \quad (14)$$

The value of R_{BVN} is analytically computed on the basis of fully-developed, steady-state Poiseuille flow across all vessels in the BVN (with the bifurcation correction term included for all relevant blood vessels). The value of R' is chosen such that the average pressure distribution across the BVN vessel size range is consistent with physiologic values (80,81). For example, for the BVN subcompartment used in this study the P* at the inlet artery diameter of 1.3 mm is ~70 mmHg. The value of R'' is then specified by equation (14).

As noted above, when a wound is present, the BVN domain is split into a 'wound' sub-network with finite resistance R_w and an 'intact' sub-network with a reduced resistance, R_{BVN}. Conservation of mass now leads to a closed-form expression for P*(t) given by,

$$P^*(t) = \frac{\frac{P_{in}(t)}{R'} + \frac{P_{atm}}{R_w} + P_{out}(t)(\frac{1}{R_{BVN}} + \frac{1}{R''})}{\frac{1}{R'} + \frac{1}{R_w} + \frac{1}{R_{BVN}} + \frac{1}{R''}}, \quad (15)$$

R_w may be computed in the same way as R_{BVN}, i.e., assuming the Poiseuille flow across all severed vessels. Note that this is a well-posed operation for any combination of severed vessels – even in the asymmetric BVN (i.e. differences in diameters/lengths of daughter vessel pairs). Imposing a mass balance at each bifurcation point and specifying the pressures at terminal vessels generates a set of linear equations of the form

$$\boldsymbol{Ap = b} \quad (16)$$

Where **A** is a sparse matrix of resistances associated with each bifurcation point, **b** is a vector with non-zero elements only where pressure boundary conditions apply, and **p** is a vector of nodal pressures and can be used to calculate the pressure distribution through the network, and subsequently flowrate and wall shear rate distributions. Since both of the geometric properties (length and diameter) and the blood viscosity (a function of diameter, and diameter is known) in each of the blood vessels is known throughout the duration of the simulation, the matrix **A** can change with time but is never undetermined. LU

decomposition with partial pivoting can be used to solve for the pressure distribution of the network, noting that this is simplified in a symmetric bifurcating network since the nodal pressures of the same generation must be the same.

2.4 Results

2.4.1 Validation

The flowrate and pressure profiles through the vascular network in the absence and presence of bleeding are shown in Fig. 2-4. In the absence of bleeding, pressure and velocity values are in agreement with in vivo measurements as shown in appendix A Figure A1 for the simulation conditions in the range of β= 6-20. (80,81). The flowrate decreases exponentially since the network is symmetric and mass is conserved at every bifurcation in the network. The pressure profile decreases linearly over the first 17 generations since each daughter vessel has approximately twice the resistance of its parent vessel when the branching exponent is ~3. Once the diameter of the vessels reaches the 5-80 μm range, however, the resistance of each daughter vessel increases more than twice the amount of its parent vessel because of the apparent viscosity increase in smaller blood vessels (82). This causes a larger resistance and pressure drop at the arteriole – capillary scale, consistent with the notion that arteriole scale blood vessels are vital for controlling arterial blood pressure (ABP).

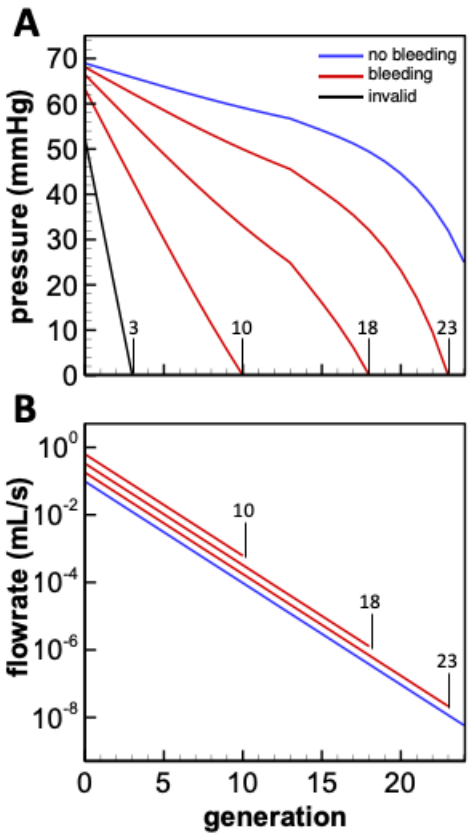

Fig. 2-4 Pressure (A) and flowrate (B) profiles in the presence and absence of acute bleeding. For complete severing at t = 0 of 2^n vessels at n = 3, 10, 18, 23 generation (**A**), network depressurization was simulated successfully for the pressure matching condition of P_{in} = 70 mmHg for wounds n = 10, 18, 23 (red curves). For n = 3, depressurization did not allow successful pressure matching and caused a hemodynamic discontinuity by not matching the P_{in} = 70 mmHg condition. For n = 10 - 25 generation wounding, the network depressurizes due to the sudden exposure to atmospheric pressure. Under all conditions of wounding, the flow rate (**B**) through the network increases relative to the intact network as a result of loss of downstream resistance (i.e., P_{out} = 0). As wounds increase in severity by severing larger vessels, the overall flowrate through the network increases 6-fold from 0.09 mL/s (no wounding) to 0.63 mL/s for n = 10 generation wounding.

To our knowledge, quantitative data is not available for human bleeding rates from defined wounds under coagulopathic hemorrhage. To validate the model of pressure-driven bleeding, simulations were performed to determine if the experimental results of Silva et al. could be reproduced (83). Silva et al. tracked cumulative blood loss and mean arterial

pressure for pressure-driven hemorrhage in heparinized dogs with specified initial blood loss rates. The initial normalized blood loss rate in the human simulation was set equal to that of the reported experimental condition in the canine model (~0.026 mL/sec per kg at t = 0). While the wounding geometries were different in the human simulation and the canine model, matching the initial bleed rate allowed accurate prediction of the dynamics of systemic blood pressure and blood volume. As bleeding proceeded for 6000 s in each case, there was strong agreement between the model and the in vivo measurements as shown in Fig. 2-5.

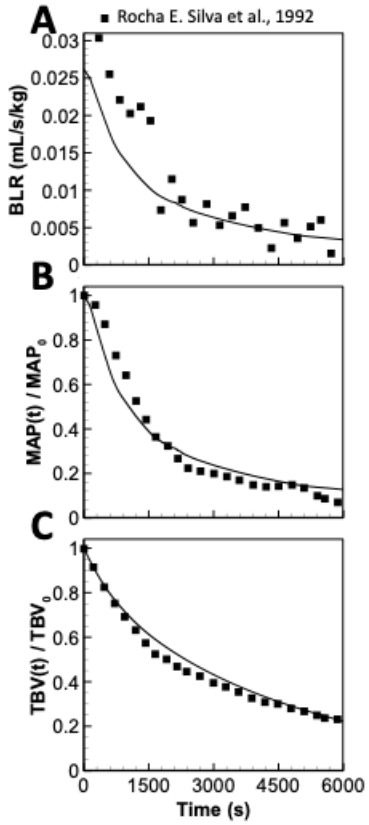

Fig. 2-5 Model validation in the presence of bleeding. Comparison of multiscale model with normalized in vivo measurements of blood loss rate (A), mean arterial pressure (B), and total blood volume (C) in heparinized bleeding dogs (83). Simulation was performed with the same initial

normalized blood loss rate as the reported experimental condition. Excellent agreement can be seen between the two. The initial total blood volume of the dog was estimated assuming a blood volume of 85 mL/kg in the dog (84) .

2.4.2 Depressurization of vessels

Blood pressure in arteries and arterioles is typically a minimum of 30 mmHg above atmospheric pressure and when one of them is severed, blood vessels near the wound site depressurize to equilibrate with the atmosphere. Consequently, the inlet pressure boundary condition cannot be set by the GH model if the root vessel is affected by the depressurization. This effect is seen in Fig. 2-4, where the pressure distribution is shown in the bleeding and non-bleeding networks. In the absence of bleeding, the pressure drop across the entire vasculature tree is 45 mmHg. Severing a generation of blood vessels leads to a pressure reduction (depressurization) that propagates up to the root blood vessel (generation 0). The pressure must be set by the global hemodynamic module upstream of the vessel sever where the effects of the local depressurization have not been felt. Directly specifying the inlet pressure boundary condition to the severed vessel would overestimate the true bleeding rate of the system since it would overestimate the pressure. For severs made at generation $n \geq 10$, the depressurization has a negligible effect on the root blood vessel (Fig. 2-4). Therefore, all wound severs described in this paper were made to 10^{th} generation blood vessels and beyond.

2.4.3 Response to vessel severing in the absence of clotting

In order to quantify the relative effect of vessel dimensions on wound severity, entire generations of vessels from the vasculature network were severed. The evolution of global hemodynamic quantities as a result of severing all the 10^{th}, 13^{th}, 18^{th}, and 23^{rd} generation blood vessels are shown in Fig. 2-6. While simulations with a fully functional baroreflex do include tachycardia and vasoconstriction, they did not include vasoconstriction of the damaged BVN unless explicitly specified to quantify its effects. Therefore, in the absence of local vasoconstriction, clotting, and external intervention of any kind, vessel severing patterns that are exposed to atmospheric pressure can be quite serious with ~1.0 – 2.4 L of blood loss predicted just 2 hours post-injury. Complete nonsurvivable hemodynamic collapse would be expected at ~2 - 2.5 L of blood loss in the absence of external intervention (85). As blood is lost from the circulatory system, arterial blood pressure (ABP) and blood loss rate (BLR) decrease since the pressure drop at the wounds decrease as mean arterial pressure decreases. Heart rate increases (Fig. 6B) as the baroreflex responds to maintain blood perfusion as blood pressure is lost.

The effect of resistance on total blood loss is also demonstrated in Fig. 2-6. The difference between all 10^{th} generation blood vessels being severed (vessels 1024-2047) and all 13^{th} generation blood vessels being severed (vessels 8192-16383) is the downstream resistance provided by the additional bifurcations. The simulation predicts that after 2 hours, this

additional resistance can prevent the loss of ~0.1 – 1.5 L of blood, a dramatic difference in blood loss over this time frame. While it has been known that resistance is imperative to maintaining hemostasis, this is the first time the effect has been quantified. Since the only way to drive blood loss rate to zero in this simulation is with decreasing blood pressure as a result of blood loss, non-survivable hemodynamic collapse is expected in all four cases in the absence of hemostasis.

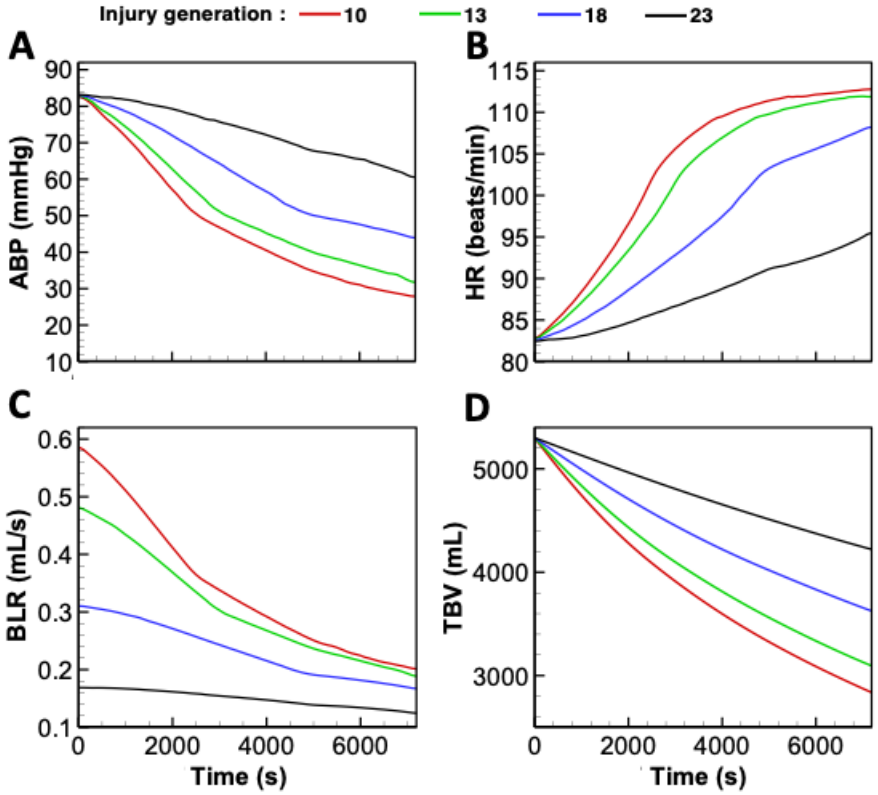

Fig. 2-6 Global and local hemodynamics following different injuries (no hemostasis). Arterial blood pressure (ABP), blood loss rate (BLR), heart rate (HR), and total blood volume (TBV) evolution as a result of severing all 10^{th}, 13^{th}, 18^{th}, and 23^{rd} generation blood vessels. A moving average was used to remove systole and diastole fluctuations in panels **A - C** for visual clarity. As blood is lost, blood pressure drops while heartrate increases due to baroreflex. The rate of blood loss declines with time as the driving force (ABP) declines. The sensitivity of bleeding to prevailing ABP is less pronounced for injury of n = 23 generation vessels due to the added upstream resistance and diameter-dependent viscosity.

Evolution of ABP, cardiac output (CO), and the cardiac cycle curve due to severing all generation 10 blood vessels are shown in Fig. 2-7. All three hemodynamic quantities suggest that the greatest change in the state of the patient occurs in the first 2000 seconds, which is when blood loss rate is highest. Both blood volume and blood pressure decrease because of blood loss explaining the shift in the cardiac cycle to the lower-left corner of the plot. In the cardiac cycle curve, the magnitude of the cardiac output pulses decreases significantly although the frequency increases, suggesting that the heart is beating faster but less efficiently to maintain blood perfusion. This can be quantified by examination of the cardiac curve, where the ratio of the area within the curve post-bleeding and prior to bleeding can be thought of as a measure of heart efficiency. After just 4500 seconds of bleeding, the efficiency of the heart has already decreased to below 20% of the non-bleeding state.

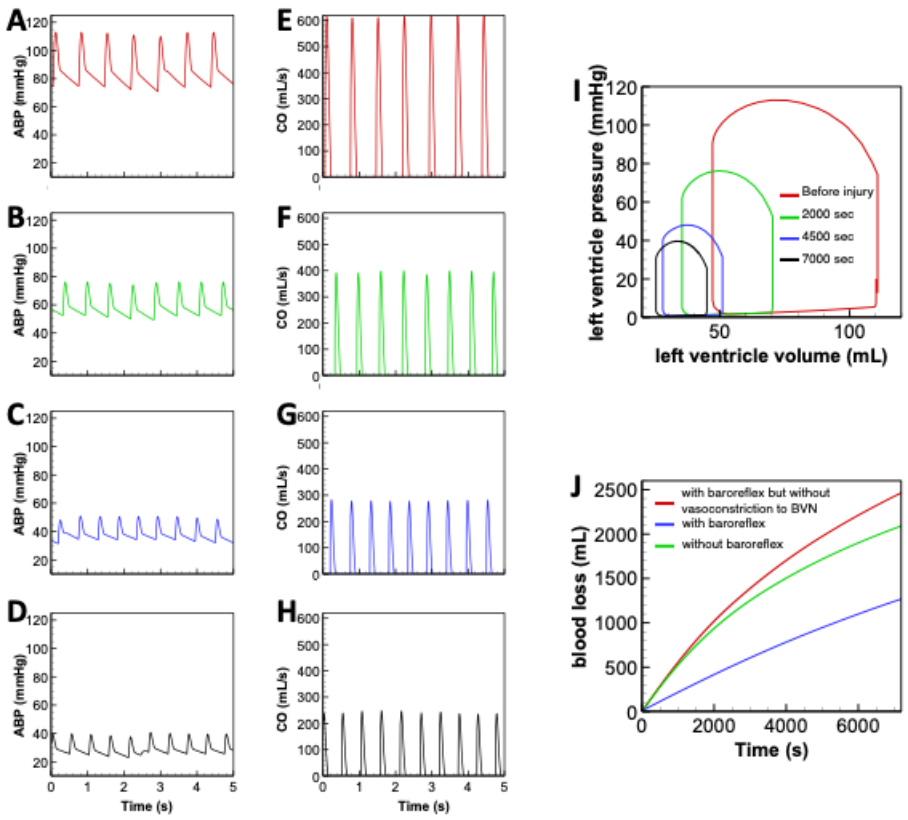

Fig. 2-7 Global hemodynamics changes in response to severing all generation n = 10 vessels at 0, 1000, 2000, and 3000 s post-injury. Panels **A-D** and **E-H** show arterial blood pressure (ABP) and cardiac output (CO) over a 5 second time interval, respectively. As bleeding occurs, the heart rate increases due to the action of the baroreflex (number of pulses in each panel increases from top to bottom). The cardiac cycle curve at the same time points is shown in panel **I** – the efficiency of the heart rapidly decreases to below 25% in less than 2 hours. All three quantities suggest that the greatest change in the state of the patient occurs in the first 1500 seconds, which is when blood loss rate is highest. The effect of the baroreflex (**J**) is quantified, where the presence of the baroreflex increases blood loss due to its attempts to maintain blood pressure during bleeding. However, if the baroreflex can still initiate vasoconstriction then the added resistance of the shrinking, bleeding, blood vessels can greatly blood loss.

In order to examine the effects of the baroreflex in maintaining hemostasis, all 10th generation blood vessels were severed and cumulative blood loss was tracked. Vasoconstriction to the local, damaged BVN was simulated by assuming vessels with diameters in the 100μm < d < 550μm range experienced a 30% diameter reduction and vessels with diameters in the 10μm < d < 100μm range experienced a 60% reduction over

1 minute, consistent with reported values (86,87). In the case where local vasoconstriction does not occur, blood loss was larger in the presence of the baroreflex than during its absence - as shown in panel J of Fig. 2-7. This can be attributed to the baroreflex's attempt to increase arterial blood pressure when it begins to decrease as a result of the blood loss. In doing so however, blood pressure increases and so does the rate of blood loss. Local vasoconstriction can dramatically increase resistance and limit bleeding, with ~ 1.2 L less blood lost over a 2-hour interval.

2.4.4 Implications of the Vasculature Network Geometry and Location

The branching exponent and the length to diameter ratio of the BVN are known to vary greatly depending on tissue or organ (88,89). Sensitivity analyses were performed on both parameters, and the root vessel diameter, to test how the geometry of the BVN can affect bleeding. A sensitivity analysis on the ratio of implicit resistances, R'/R'', was also performed in order to test how sensitive the blood loss rate was to the pressure of the root vessel. Fig. 2-8 shows the sensitivity analysis results of all four quantities by plotting cumulative blood loss during the first hour of bleeding in the absence of clotting and as a result of all 10^{th} generation blood vessels being severed. Interestingly, blood loss was found to be highly sensitive to all parameters, especially branching exponent where a minor increase in the branching exponent can drastically increase the amount of blood lost. This suggests that location of the injury can be a large determinant in injury severity. Blood loss predictions for 1000 simulations when this parameter is randomly chosen between 2 and 3

at generation for the entire network is shown in Fig. A2, further highlighting its significance.

The sensitivity to the ratio, R'/R'', suggests that the type of vessel can be a strong indicator of injury severity, with wounds to high pressure vessels being significantly more severe.

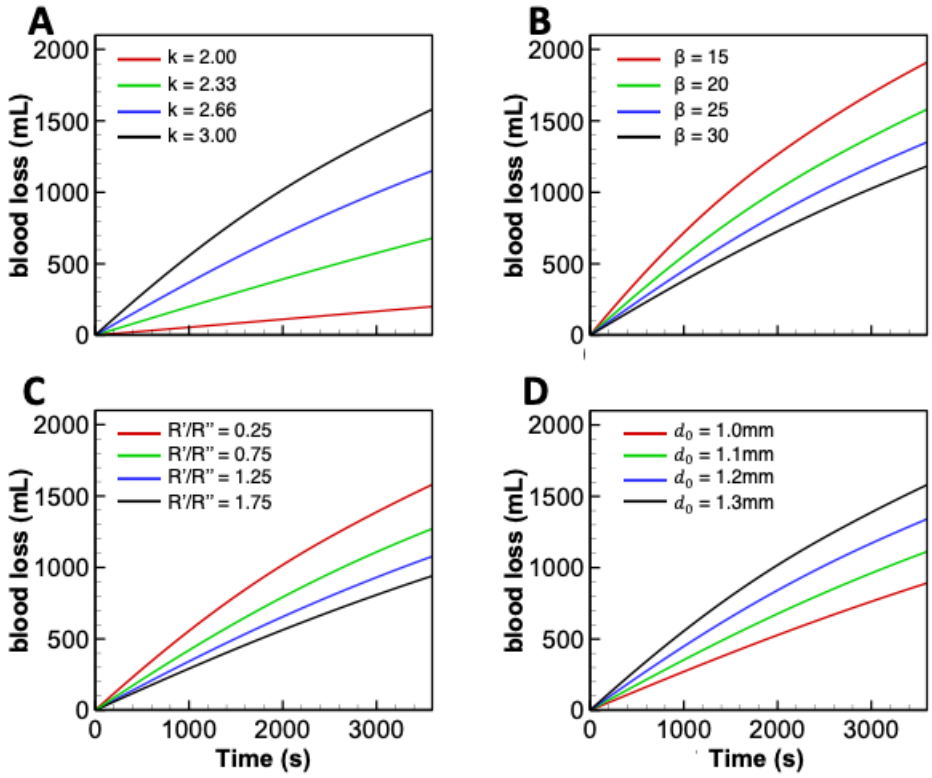

Fig. 2- 8 Effects of network properties on blood loss. Blood loss profiles for n = 10 wound in the absence of hemostasis due to changes in: branching exponent, k (**A**), the length/diameter ratio, β (**B**), the ratio, R'/R'' (**C**), and root diameter at n = 0, d_o (**D**). The branching exponent has the strongest effect on bleeding as downstream diameters are larger (less resistance) at larger values of K.

2.4.5 Effect of hemostatic closure of severed vessels

The effects of clotting on the bleeding outcome of the patient were simulated by assuming fully functional platelets in a healthy patient and hemodilution in a trauma patient. For simplicity, all of the mechanistic steps involved in simulating blood coagulation and platelet adhesion were not included. Rather, a parameterization of measured clot growth rates as a function of shear rate for healthy, whole blood perfused over pyrex was imposed on the damaged blood vessels (72,90). Instantaneous seal rates could then be used to compute cumulative blood vessel diameter changes as a result of the clotting. The parametric relationship is:

$$S = \frac{dD}{dt} = \begin{cases} 2 * \frac{1.7\gamma^{0.30} - 3}{60}, \gamma \leq 5999s^{-1} \\ a_2\gamma^2 + a_1\gamma + a_0, 5999s^{-1} < \gamma < 8564s^{-1} \\ 2 * \frac{34 - 1.1\gamma^{0.28}}{60}, \gamma \geq 8564s^{-1} \end{cases} \quad (17)$$

where S is sealing rate (μm/s), γ is wall shear rate (1/s), and a_2, a_1, and a_0 are fitted coefficients to smooth the sharp bifurcation between the other two power law fits. Their values are $a_2 = 2.405*10^{-8}$ μm*s, $a_1 = 3.502*10^{-4}$ μm, and $a_0 = -0.565$ μm/s. Wall shear rate was calculated with the standard formula:

$$\gamma = \frac{32Q_i}{\pi(d_i)^3} \quad (18)$$

where the subscript i references the specific blood vessel. In a circular cross-section, seal rate was assumed to be twice the clot height growth rate and vessel clotting was assumed to take place over the entire length of the blood vessel. The response curves as a result of all 10^{th} generation blood vessels being severed are shown in Fig. 2-9. Loss of downstream resistance caused wall shear rate to mediately increase to ~$\boxed{10^3}$ s^{-1}. As the severed blood vessel seals due to hemostatic clotting, wall shear rate further increased to 3-5x the initial value. However, once clot growth had substantially reduced the available lumen, the pressure drop became large enough to significantly reduce wall shear rate, seal rate, and blood loss rate. After just 100 seconds post-wounding, full hemostasis was achieved. The action of the baroreflex can be seen to have a positive effect on simulations, where local vasoconstriction reduces blood loss by ~40 mL.

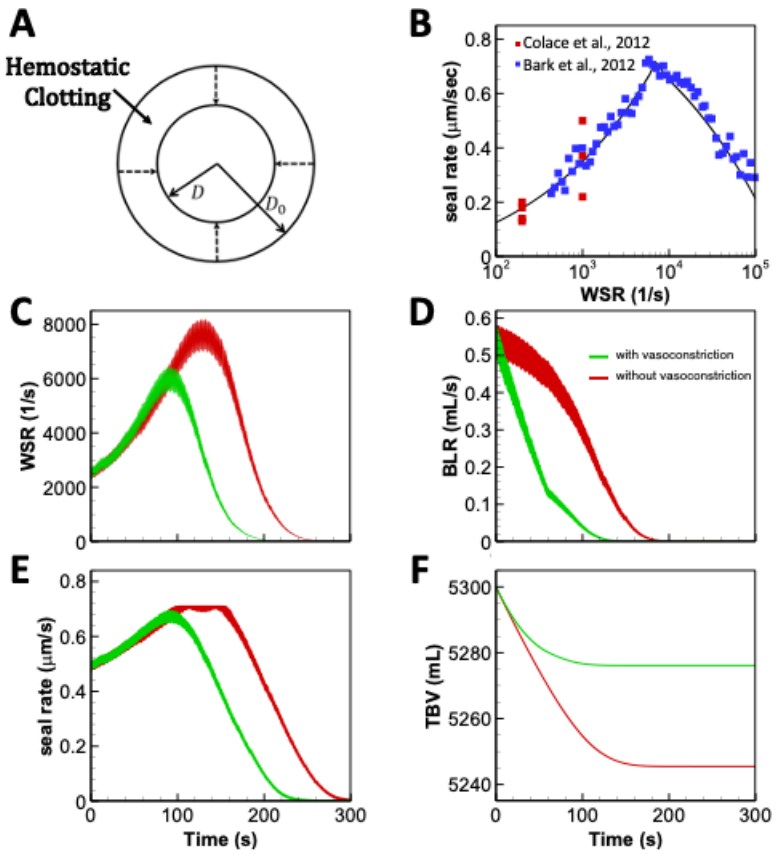

Fig. 2-9 Global and local hemodynamics with healthy hemostasis. Uniform clotting occurs over the entire length of the severed blood vessel (**A**) reducing the initial diameter of the blood vessel (D_o) to the effective diameter (D) at a rate given by the seal rate – wall shear rate function parameterized by the experimental measurements of Colace et al. (72) and Bark et al. (90) (**B**) . Wall shear rate (**C**), blood loss rate (**D**), seal rate (**E**), and total blood volume (**F**), evolution as a result of severing all generation 10 vessels in the presence of shear-dependent clotting. The effect is dramatic, with blood loss ceasing just ~100 seconds into the simulation.

Fig. 2-9

Hemodilution was simulated by running simulations with different hematocrits. This required modification of the seal rate–shear function since hematocrit is known to be a strong modulator of clot growth rate via driving platelet margination as well as altering the wall shear rate. The seal rate - shear rate function shown in Fig. 9B was rescaled by

hematocrit (h) according to the measurements of Li et al. (91) (Insert of panel C Fig. 2-10). Simulations at h = 0.23, 0.30, and 0.45 (Fig. 2-10) demonstrated the risk of low hematocrit, with clotting time and total blood loss being an order of magnitude larger for h = 0.23 compared to h = 0.45. Furthermore, since blood viscosity is a function of hematocrit, the blood loss rate increased by a factor of ~2 as hematocrit decreased. In all three cases, wall shear rates continue to reach ~10^4 s^{-1}, suggesting that vWF elongation can occur during traumatic bleeding even with vasoconstriction and hemodilution. These results suggest that hematocrit changes as a result of transcapillary refill could contribute to TIC via hemodynamic mechanisms.

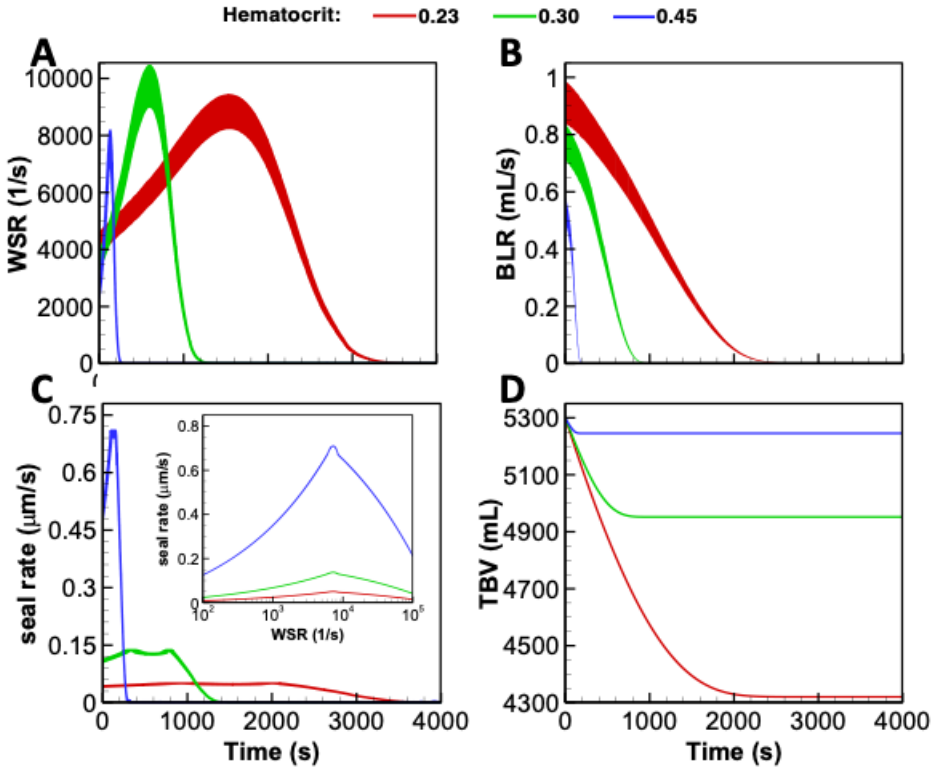

Fig. 2-10 Global and local hemodynamic evolution for different hematocrits. Wall shear rate (**A**), blood loss rate (**B**), seal rate (**C**), and total blood volume (**D**), evolution as a result of severing all generation 10 vessels in the presence of shear-dependent clotting and for different hematocrits. Local vasoconstriction was not included to examine the sole effect of the hematocrit change. Seal rate function rescaled by data presented by Li et al. (91). While all three have similar wall shear rate profiles, total blood loss dramatically increases by ≈1L as a result of a 2-fold decrease in hematocrit. This suggests that hemodilution could be a large component of trauma induced coagulopathy (TIC).

2.5 Discussion

A bleeding bifurcating vasculature network (BVN) model was coupled to a global hemodynamic (GH) model in order to predict the bleeding trajectory of a patient in response to defined tissue injury. This is the first computational model to relate wound geometry on the microvascular scale to global hemodynamic changes in a patient.

Furthermore, the dimensionality of the GH model is unaltered by incorporation of the BVN thus preserving its computational efficiency.

The simulations emphasized the importance of vascular network depressurization, vascular geometry, and local hemodynamics. The model predicted that patient trajectories were highly dependent upon the geometry of the bleeding vasculature network, in particular the branching exponent, k, and the length to diameter ratio, β. Patient outcome may be highly dependent upon wound location since these parameters are known to vary significantly in the body. The simulation results presented in this paper were all generated using $k = 3$ and $\beta = 20$ (except during sensitivity analyses). With a symmetric bifurcation and a constant rotation angle of 60°, it is possible to calculate an order of magnitude approximation of the volume spanned by the BVN. Severing all generation 10 vessels would roughly correspond to a $10cm^3$ (2cm * 2cm * 2.5cm) and since each finger is known to contain 2 palmer digital arteries, generation 10 severs should roughly correspond to severing the end of a fingertip.

A coarse-grained hemostasis function was used in this study. Future work can use full simulation of clotting (59) based upon platelets from trauma patients (92). Alternatively, microfluidic measurements of clot growth using coagulopathic blood is possible (91). Importantly, the simulations predicted pathologically high wall shear rates on the order of $10^4\ s^{-1}$. Colace et al. (73) and Herbig et al. (74) demonstrated that human Von Willebrand Factor (VWF) multimerizes at shear rates of these orders of magnitude suggesting that

wounds of these sizes and pressures can lead to VWF unfolding and fiber formation. One of the challenges associated with incorporating clotting under flow models is the associated computational cost and lack of 3D simulations at the arterial length scale. Furthermore, it is well-established that platelets in the traumatized patient are highly dysfunctional (93), so standard models of platelet aggregation will need to be augmented to account for this.

Furthermore, an important emergent result is the phasic nature of the response to bleeding in the presence of clotting. The wall shear rate function shows an initial jump in wall shear rate to $\sim 10^3\ s^{-1}$ due to the loss of downstream resistance and increased flow rate. Afterwards, the wall shear rate in each blood vessel continues to increase as the platelet accumulation reduces the effective diameters of the wounded blood vessels. Once the diameters of the bleeding vessels reach a critical value, the clotting is sufficiently advanced to reduce blood loss rate, seal rate, and wall shear rate. Note that this model does not include the well-known effect that clot growth experiences an initial delay during in vitro experiments involving blood perfusion over a collagen/tissue factor surface; there is a need for an initial layer of platelets to aggregate before significant clotting can begin. This effect can be captured with a more complex model for clotting under flow (54,57,59).

Limitations of this model can originate from several sources, including the global hemodynamic model, the vascular network, the multiscale coupling between them, or neglection of some of the mechanisms for maintaining hemostasis.

The first potential limitation of the global hemodynamic model is its lumped parameter representation of a component of the vasculature. Milisic and Quarteroni et al. have provided a proof that the lumped parameter methods used in 0D models of the circulatory system are first order discretization's of 1D models of the cardiovascular system (94). While a more complex model that uses higher order discretization would be able to capture the pulse-wave transmission effects, these would not affect the evolution of blood pressure, heart rate, and blood loss rate and only add computational cost to simulations. Therefore, the authors concluded that a standard 0D global hemodynamic model would be appropriate for this study. Note that 2D and 3D models of regions of particular interest can also be coupled to 0D or 1D GH models, although this was not needed for this particular study (95–97).

Platelet and endothelial dysfunction, anticoagulation, hyperfibrinolysis have all been implicated during major trauma, an effect known as trauma-induced coagulopathy (TIC) (93). The simulations in this model were relatively short (< 2 hours) and the timescale for TIC is on the order of many hours. On the other hand, longer simulations would require careful consideration of TIC where both variable hematocrit and impaired platelet aggregation would need to be included. The BVN also makes several assumptions about the geometry of the vascular network for simplicity. The first assumption is parabolic flow through rigid, cylindrical, blood vessels. While this is generally a fair assumption, arteries

and arterioles may be quite compliant and easily deformable with ~40% changes in diameter and non-circular, non-constant cross-sectional shape across the entire length of the blood vessel. This assumption leads to inaccuracies in vessel resistance calculations, in general underestimating them. However, while the resistance through an individual blood vessel is uncertain, the overall resistance of the BVN is more accurately calculated (79). Since vessel severs were made a minimum of 10 generations from the root vessel, an accurate resistance for the bleeding BVN is still computed.

The multiscale coupling strategy extracts the vascular network model from a lumped representation of a component of the cardiovascular system. The local depressurization effect however creates a significant limitation in the bleeding patterns that can be simulated. The vascular network requires the pressure be set by the global hemodynamic model, however the depressurization makes it impossible to set the pressure independent of this effect. It is not possible to completely extract the entire lumped parameter into constituent blood vessels as this would be too computationally expensive, so wound severs must be made a minimum of 10 generations from the root vessel to minimize this error. Of course, this limits blood loss patterns predictable by the model as it not possible to sample from earlier generations.

The contribution of this work is a model that efficiently predicts the hemodynamic response to severing blood vessels from the single vessel scale to the global hemodynamic response

as well presents a multiscale coupling strategy for efficient simulation. The developed coupling strategy is one that can be used for coupling all lumped parameter models, so long as knowledge on the magnitudes of the correct inlet and outlet boundary conditions to the resolved model are available. It also directly addresses depressurization as a result of blood vessel severing, an effect that is often overlooked and must be addressed to correctly predict patient trajectories.

CHAPTER 3: USING THE NATIONAL TRAUMA DATA BANK AND MACHINE LEARNING TO PREDICT PATIENT MORTALITY AT ADMISSION

3.1 Abstract

A 400-estimator gradient boosting classifier was trained to predict survival probabilities of trauma patients. The National Trauma Data Bank (NTDB) provided 799233 complete patient records (778303 survivors and 20930 deaths) each containing 32 features, a number further reduced to only 8 features via the permutation importance method. Importantly, the 8 features can all be readily determined at admission: systolic blood pressure, heart rate, respiratory rate, temperature, oxygen saturation, gender, age and Glasgow coma score. Since death was rare, a rebalanced training set was used to train the model. The model is able to predict a survival probability for any trauma patient and accurately distinguish between a *deceased* and *survived* patient in 92.4% of all cases. Partial dependence curves ($P_{survival}$ vs. feature value) obtained from the trained model revealed the global importance of Glasgow coma score, age, and systolic blood pressure while pulse rate, respiratory rate, temperature, oxygen saturation, and gender had more subtle single variable influences. Shapley values, which measure the relative contribution of each of the 8 features to individual patient risk, were computed for several patients and were able to quantify patient-specific warning signs. Using the NTDB to sample across numerous patient traumas and hospital protocols, the trained model and Shapley values rapidly provides quantitative insight into which combination of variables in an 8-dimensional space

contributed most to each trauma patient's predicted global risk of death upon emergency room admission.

3.2 Introduction

Trauma is the third leading cause of mortality in the United States and results in approximately 6 million deaths and a cost over 500 billion dollars worldwide each year (60,98). A unique characteristic of trauma in relation to other diseased states is not only the large patient-to-patient variability, but non-physiological considerations such as the distance from a trauma center, the resources available for resuscitation, and the number of other casualties. These additional complexities make patient risk analysis difficult, but necessary, to implement in real time. Given the intricacy of traumatic injury, patient-scale modeling of trauma from first principles is extremely challenging. Consequently, machine learning approaches have been the mainstay of modeling in this arena. In this regard, a large and diverse data set is valuable for the training of an accurate model to efficiently predict patient risk, warning signs, and survival probabilities from easily measurable or estimable quantities.

Trauma centers prioritize patients as they arrive by dividing them into various tiers based upon patient vital signs (respiratory rate, systolic blood pressure, etc.), nature of the injury (i.e., penetrating), and Glasgow Coma score (99). This prioritization is essential, as it is understood that the sooner a patient receives surgical or medical treatment the greater the likelihood for patient survival (100). A well-trained model has the potential to help in this patient prioritization by providing a quantitative metric for patient risk. Moreover, the use of SHAP values (101), for example, to explain the prediction of the model may help alert the clinician of difficult-to-discern combinatorial risks in a high dimensional pathophysiological space.

To date, neural networks have been the primary model in the study of trauma. Edwards and Diringer et al. showed that a neural network could accurately classify mortality in 81 intracerebral hemorrhage patients (102). Marble et al. used a neural network to predict the onset of sepsis in blunt injury trauma patients with 100% sensitivity and 96.5% specificity (103). Estahbanati and Bouduhi used neural networks to predict mortality in burn patients to a 90% training set accuracy (104). DiRusso et al. compared the accuracy of logistic regression (linear) and neural networks (non-linear) in predicting outcomes in pediatric trauma patients (105). Walczak used neural networks to predict the transfusion requirements of trauma patients, an important problem considering potential resource limitations and adverse responses (106). Mitchell et al. used comorbidities, age, and injury information to predict survival rates and ICU admission (107). Recently, Liu and Salinas published an extensive review on how machine learning has been used in the study of trauma (108). In general, studies have focused on the capability to predict mortality, hemorrhage, and hospital length of stay. The datasets used in these studies generally came from local trauma centers and varied greatly in training and test set size, with most studies on the order of hundreds of patients and some on the order of thousands (103,109). Models based on ordinary and partial differential equations have also been used to study trauma but were not used in this report (6,7,20,110,111).

Here, we take a machine learning approach based on a gradient boosting classifier (112) for predicting survival probabilities. Furthermore, we make use of Shapley values to garner a physiological and quantitative understanding of why patients are either at high-risk or low-risk. With a reasonably small set of 8 easily measurable and commonly known

features, we demonstrate accurate prediction of patient survival probabilities and the ability to indicate patient warning signs.

3.3 Methods

3.3.1 Patient Dataset

All training and testing data was obtained from the National Trauma Data Bank (NTDB), the largest aggregation of trauma data ever assembled in the United States (113) . The 2016 NTDB dataset was used for all training and testing and consisted of 968665 unique patients. Each patient was identified by a unique incident key with comorbidities, vital signs, and injury information, present in separate .csv files. The open-source library, *Pandas*, was used to import, clean, and merge each of the csv incident files and generate a matrix of features and a vector of outcomes. Input features consisted of binary categorical features (e.g., gender, alcohol use disorder, etc.) and numerical features (e.g., age, systolic blood pressure, heart rate, etc.) while the outcome vector consisted of the binary *states, survived or deceased.*

3.3.2 Preprocessing

Of the 968,665 unique patients in the trauma database, 351,253 patients contained missing data. The death rate of the population of patients with missing data was 1.4 times greater than that of the patients without, suggesting that patients with missing data should not be ignored. Therefore, we used an iterative imputation method (see supplemental section for details) to impute the missing values of all patients missing 2 or fewer features. This threshold was chosen based on the distribution of quantity of missing features, which is

shown in supplemental Fig. B1. This captured 181,821 additional patients, and the death rate of all included patients was now approximately equal to that of the excluded patients.

Commonly presenting categorical features (hypertension, alcoholism, etc.) that were initially present in the comorbidities .csv file were encoded into their own binary columns, indicating whether a patient had the preexisting comorbidity or not. Continuous variables such as vital signs were also included. The feature matrix, **X**, is NxM dimensional where N is the total number of patients and M is the total number of features used to construct the model. All feature values in the feature matrix were rescaled to be between 0 and 1 by the minimum and maximum of each feature, i.e.,

$$\boldsymbol{X\_s}_{:,j} = \frac{\boldsymbol{X}_{:,j} - \min\left(\boldsymbol{X}_{:,j}\right)}{\max\left(\boldsymbol{X}_{:,j}\right) - \min\left(\boldsymbol{X}_{:,j}\right)}, \tag{1}$$

where $\mathbf{X\_s}_{i,j}$ is the rescaled j^{th} column in the new feature matrix and $\mathbf{X}_{:,\text{j}}$ is the unscaled j^{th} column of the original feature matrix. Feature rescaling is a standard preprocessing step performed so that all features are dimensionless and of the same order of magnitude.

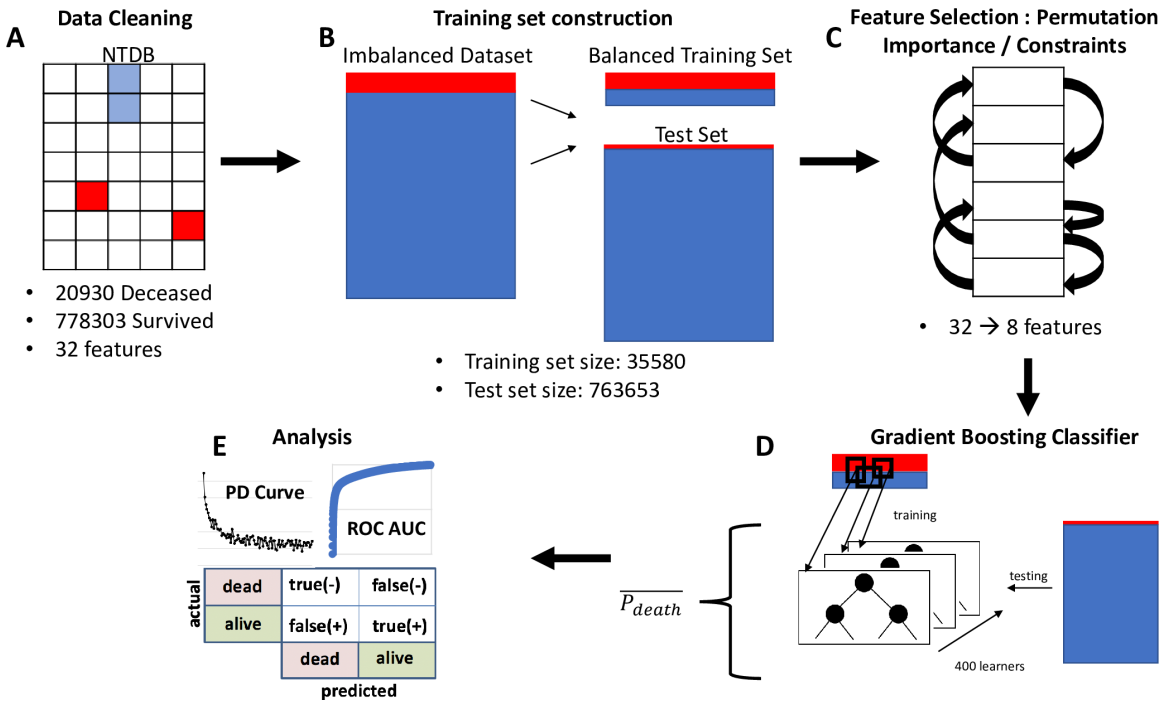

Fig. 3-1 Process Flow Diagram of the process of building a predictive trauma model. The dataset is acquired from the National Trauma Data Bank (NTDB) and any patient with more than 2 missing data fields were removed from the dataset (cleaning). The data consisted of relational tables with each patient identified by a unique incident key. By merging using the incident key, it was possible to generate a matrix of data where each row represented a unique patient and each column represented a unique feature. Features were included in the column based on physiological information that was expected to contribute to the outcome of the model. This included age, gender, vital signs, coma and severity scores, and comorbidities. Facility and demographic information (other than age) was not included in the analysis. The dataset was then divided into a balanced training set (equal number of survived and deceased patients) and a test set, a model was trained on the training set with optimized hyperparameters (see appendix Fig. B2), and then the results reported and analyzed.

3.3.3 Class Imbalance

One of the challenges associated with classifying whether the patient *survived* or *deceased* is that the dataset had 778303 *survived* patients and only 20930 *deceased* patients, a very large class imbalance (114). We chose to address this problem by undersampling from the *survived* class. A total of 85% of the *deceased* patients were randomly selected to be included in the training set, and an equal number of *survived* patients were randomly selected to be included in the training set. All other patient records were included in the

test set resulting in a training set of size 35580 records and a test set of size 763653 records, as shown in Fig. 1B.

3.3.4 Feature Selection

A critical step in determining the final accuracy and utility of the model in the trauma unit (i.e., bedside) was determining which features to include. In this study, features were chosen not only based upon which would be the most predictive of outcome but also upon which would be the easiest to measure on admission. The permutation importance (PI) method (115) was used to determine which features were most likely to be the most predictive of trauma, see Fig. 3-1C. The method consists of training a model, obtaining an accuracy for that model on the independent test set, then randomly permuting each feature column and measuring the change in accuracy. If the accuracy of the model decreases significantly, then this implies that the permuted feature was heavily contributing to the prediction of the model and should be kept in the final model.

In this case, the PI method guided the reduction of 32 feature to only 8 final features per patient record. The final 8 features used for model training were: systolic blood pressure (SBP), heart rate (HR), respiratory rate (RR), temperature (Temp), oxygen saturation (SaO2), gender, age, and total Glasgow coma score (GCSTOT). The full list of features before and after the reduction can be found in supplemental Table 3-1. While the Glasgow Coma Score can be unreliable in intubated patients, only an exceedingly small percentage (<1%) of the entire NTDB trauma patient set were in that state (116).

Table 3-1: Table of all features used to make predictions.

32 features	8 features

GCSTOT	GCSTOT
Age	Age
HR	HR
SBP	SBP
TEMP	TEMP
GENDER	GENDER
RR	RR
SaO2	SaO2
Advanced Directive Limiting Care	
Alcohol Use Disorder	
Attention Deficit Disorder	
Bleeding Disorder	
Cerebrovascular Accident	
Chronic Obstructive Pulmonary Disease	
Chronic renal failure	
Cirrhosis	
Congenital Anomalies	
Congestive Heart Failure	
Current Smoker	
Chemotherapy for cancer	
Dementia	
Diabetes Mellitus	
Disseminated Cancer	
Drug use disorder	
Functionally Dependent	
Peripheral Vascular Disease	

History of Angina

History of Myocardial infarction

Hypertension

Major Psychiatric Illness

Prematurity

Steroid Use

Our description of the gradient boosting classifier, partial dependence curves, and SHAP values can be found in the supplemental section.

3.3.5 Gradient Boosting Classifier

Many different machine learning algorithms exist for identifying trends and hidden patterns in a large, high dimensional dataset like the NTDB. Since the NTDB contained labeled data (i.e., *survived* and *deceased*) we focused on supervised learning approaches. This class of machine learning algorithms (e.g., support vector machine, neural network, random forest, etc.) learn a function that maps a high dimensional input to an output. Here, we choose a gradient boosting classifier because it was found to be the most accurate when compared with several other models; see Appendix Table B2. The gradient boosting algorithm utilizes a stage-wise addition of weak learners, small decision trees (stumps), and averages the prediction of each of them to make a final decision on the individual patient. During the training process, subsequent learners are trained with an added weight on the individual samples that have been classified incorrectly, as shown in Fig. 3-1D.

Most machine learning algorithms contain hyperparameters, which are parameters that must be specified prior to the start of the training process. The *k*-fold grid-search cross validation method was used to determine the optimal set of hyperparameters (number of weak learners, learning rate, the fraction of the data used for training by each learner, and the number of features to consider at each split point) for the gradient boosting classifier. The training set was temporarily subdivided into 5 folds ($k = 5$) and the model was trained with 4 of the folds and evaluated on the 5th fold. The accuracy was recorded and repeated, each time changing which fold the model was evaluated on, and the final accuracy was taken as the average of each of these. This process was repeated for each combination of hyperparameters and whichever combination produced the smallest error rate was taken as the optimal set. The validation set was returned to the training set and the model was trained and evaluated on the test set with the parameters determined to be the most optimal by the grid-search cross validation method. Note that the test data was not used during the *k*-fold grid search or the model training. A visual description of this process is shown in Appendix Fig. B2 and an example of a single weak learner from the trained model is shown in Appendix Fig. B3.

3.3.6 Global Feature Dependencies - Partial dependence

Once a model has been trained and tested, partial dependence curves on each feature can be used to garner a greater understanding of how the model depends upon each feature. Partial dependence is the marginal effect that a feature has on the model's prediction and can be used to show the form of the dependence (linear, exponential, monotonous, etc.)

and whether the feature affects the prediction positively or negatively. The partial dependence function is defined as

$$f(x_i) = \int f(x_i, x_R) dx_R, \tag{2}$$

where $f(x)$ is the trained model, i is the feature of interest, x_F is the vector of values for feature F, R is the set of all remaining features, and x_R is the dependence of $f(x)$ on the remaining features. Since the partial dependence curves are constructed by marginalizing over all remaining features, the resulting model is a function of feature i only. We can approximate this integral by discretizing equation (2), e.g.,

$$f(x_F) = \frac{1}{n} \sum_{i=1}^{n} f\left(x_i, x_R^{(i)}\right), \tag{3}$$

where n is the number of samples in the training set. This is a sensitivity analysis averaged over all test set examples. Since this method marginalizes over all features, a requirement is that feature i must be uncorrelated with the features in R. All Pearson correlation coefficients were < 0.6, verifying this assumption.

3.3.7 Patient Specific Feature Dependencies - Shapley Additive Explanations (SHAP)

While partial dependence curves provide a global view of the effect of each feature, Shapley Additive Explanations (SHAP) is a method for calculating the relative importance of each feature on a single prediction (patient)(101,117,118). The method was largely inspired by Lloyd Shapley's work in cooperative game theory, where individual players are rewarded based upon their contributions in a collaborative game (119). When applied analogously to the prediction of a model, the SHAP value measures how much each feature contributes to its prediction. This feature importance tool has the advantage of accounting for local patient-to-patient variations, which is important since a significant factor for one patient may not be for another. By contrast, global feature importance metrics, such as partial dependence curves, average out variations across the entire population.

Analogous to linear regression, the SHAP method locally approximates the function, $f(x)$, by a linear combination of the features each weighted by a SHAP value (φ), i.e., its contribution to the model prediction. Intuitively, the SHAP value of a feature is the difference in the prediction of the model with and without the feature present. While the model requires 8 inputs to run in general, it can be allowed to run by computing a weighted average of all nodes that depend upon the missing feature. The SHAP value computation of a feature, i, requires averaging the output of the model, f, for all possible subsets of features with and without i. Formally, the SHAP value is computed with the formula,

$$\varphi_i(x) = \sum_{S \subseteq N \setminus \{i\}} \left(\frac{|S|(M - |S| - 1)!}{M!} \right) * \left(f_x(S \cup \{i\}) - f_x(S) \right), \quad (4)$$

where S is the set of features being considered, $|S|$ is the cardinality of S, M is the total number of features, f_x is the prediction made by the model, N is the set of all input features, and $\varphi_i(x)$ is the shapley value of the i^{th} feature of patient x. Intuitively, the second term in equation (4) represents the importance of a feature as the difference in the prediction with and without that feature present, weighted by the first term. More information on this computation can be found in the original work by Lundburg et al. (101).

3.3.8 Iterative Imputation

We used the IterativeImputer class from the scikit-learn library to impute missing data in patients missing 2 or fewer features (120). Missing features are modeled as functions of present features and a ridge linear regression model is trained to predict the missing value. At a single step in the iteration, a single feature is treated as the missing output while the remaining features are the input. This is repeated for each feature in a single round, and then iterated for 50 rounds. In the rare instances that this imputation led to unphysical values (e.g., age < 0), we simply imputed the value with a nearby physical value. This is superior to simply imputing the missing value with the mean of the present features as it imputes the average over many approximations of possible values. Furthermore, simple imputation significantly model variance leading to lower generalizability.

3.4 Results

The accuracy of the model is expressed as the area under the receiver operating characteristic curve coefficient (AUC). Given two patients, one *survived* and one *deceased*, the AUC represents the relative likelihood of the classifier predicting that the patient who survived had the higher probability of surviving. An AUC of 0.50 is the worst-case, as it implies that the classifier is no better than random guessing while an AUC of 1.0 is the best case, as it will always classify the two patients correctly. The AUC method is also relatively insensitive to the class imbalance between the *survived* and *deceased* patients making it a logical choice as the metric for accuracy. The gradient boosting model was able to achieve an accuracy of 0.924.

In other words, with a single 8-feature vector consisting of age, gender, five vital sign measurements, and the easily measurable Glasgow coma score, it was possible to predict the outcome of the patient up to ~92.4% accuracy, making this a useful tool for quantifying patient risk. Using 32 features per patient for model training resulted in minimal improvement of the AUC (black line, Fig. 3-2). Importantly, the high accuracy of the model implies that a single snapshot view (8 features) can give a quantitative prediction of the patient's mortality risk *on admission*. For further validation, we tested the model on the 2017 Trauma Quality Programs participant use file (TQP PUF). The dataset consisted of an additional 648192 complete patient records and our model was able to achieve an accuracy of 91.2%, further validating the robustness of the model and eliminating concerns of data leakage and biased evaluation. The high accuracy on a completely different cohort of patients is perhaps unsurprising given that the data points from the NTDB represent patients from numerous trauma centers. As we show below, the utility of the model is not

only in its prediction of mortality risk, but also in its insight in quantifying key metrics that could be viewed as potential warning signs in a trauma setting.

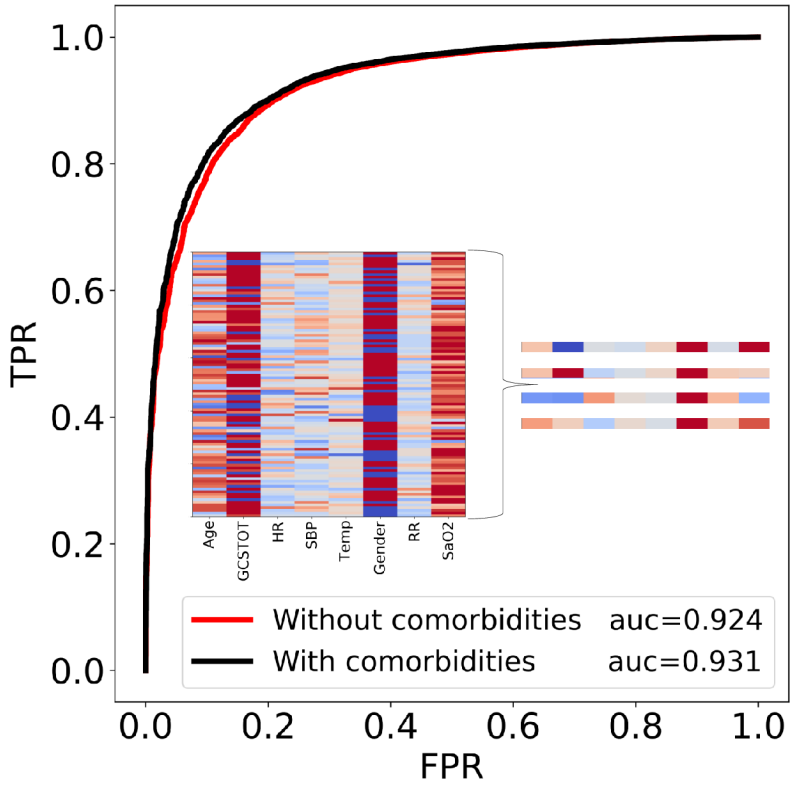

Fig. 3-2 The receiver operating characteristic curves (ROC) for 2 different cases. The true positive rate (TPR) is plotted on the y-axis and the false positive rate (FPR) is plotted on the x-axis for classification thresholds between 0 and 1. In the red curve, only 8 easily measurable vital signs or scores were included in the prediction while the black curve included these and the comorbidities. A full list of features in each case can be found in supplemental Table S1. All results are reported using the second case because the required inputs can be measured rapidly, while knowledge of the comorbidities of a patient is less likely. The heat map in the insert plots the 8 feature values of 100 randomly selected patients, illustrating the high dimensionality of the problem. While no obvious pattern can be seen by humans in the heat map, the algorithm is able to find and quantify one. 4 zoomed-in examples are provided for clarity. Note that each column is normalized by its own feature value range.

The partial dependence curves are shown in Fig. 3-3. Age, GCSTOT, and systolic blood pressure all display substantial influence on the probability of survival. The model predicts that by the age of ~60, a patient's "youth protection" has substantially dissipated on average and ages greater than this will further reduce the probability of survival. Likewise, a

GCSTOT below 12 will increase the likelihood of death. More interestingly however, is the apparent threshold behavior in the heart rate and blood pressure profiles. The probability of survival begins to drop dramatically if the SBP < ~110 mmHg or the HR > ~100 beats per minute, consistent with the findings that hypotension is correlated with higher mortality rates (121–123). The two variables are related to one another via the baroreflex, a negative-feedback loop system that increases heart rate in response to the loss in blood pressure, which will decline as blood volume is lost from the injury. Both vital signs should be viewed in tandem to assess patient status during resuscitation.

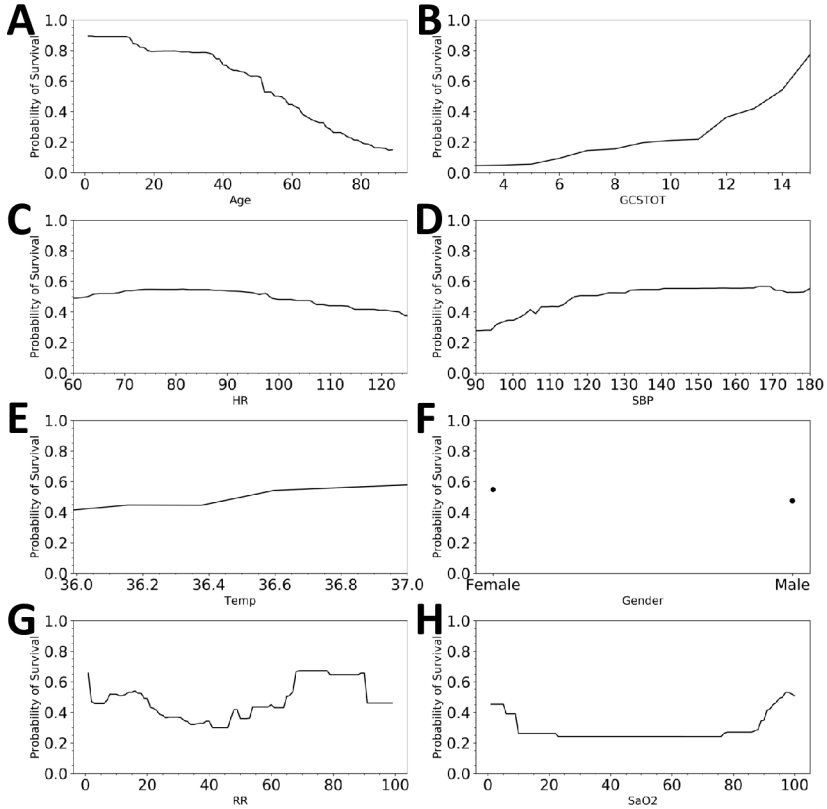

Fig. 3-3Partial dependence curves showing how the prediction of the model is globally influenced by each of the features. Pulse rate and systolic blood pressure display threshold behavior, where the probability of survival can decrease at HR > 100 beats / min and SBP < 110mmHg (123).

The probability of survival model predictions for *deceased* and *survived* patients were plotted on histograms in Fig. 4 for a visual representation of the effectiveness of the model. The distributions of survival probability had means of 0.21 (*deceased*) and 0.78 (*survived*) and were highly skewed (1.51 and -1.38, respectively) suggesting that the model was very confident in the predictions that it made.

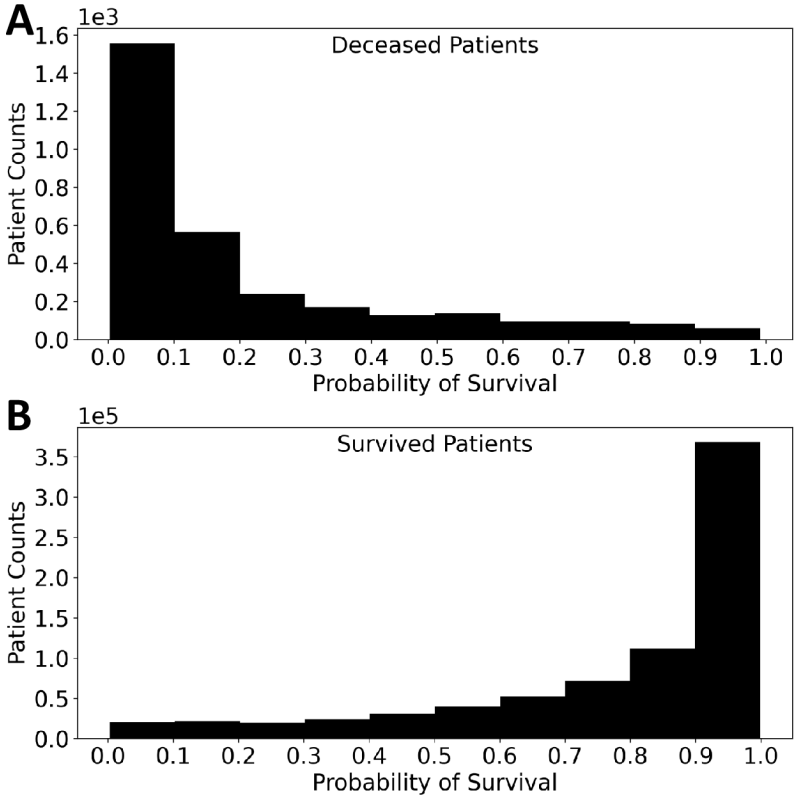

Fig. 3-4 Histograms of the survival probabilities for survived and deceased patients. If probabilities of death greater than 20% are marked as high risk, then ~96% of the deceased patients would been labeled.

Next, SHAP values were used to examine individual patient records and quantify patient risk. As examples, 4 cases are shown in Fig. 3-5. Note that the scales of Fig. 3-5 are expressed as the log-odds ratio of the probability of survived to probability of deceased (i.e., $\log(\frac{p_{surv}}{1-p_{surv}})$). A log-odds ratio of 0 ($P_{surv} = 0.5$) was used to binarize the patients into

survived and *deceased* patients. With this metric, the model correctly predicted all 4 patient outcomes in Fig. 3-5. The force plot of the SHAP values of each feature identifies the relative contribution of each variable, both positively (blue) and negatively (red). In panel A, while the patient was conscious (GCSTOT = 15) and had relatively normal heart and respiratory rates, his low blood pressure and age were quantifiably more significant and the reason the model predicted *deceased* (sum of SHAP values < 0). In case B, the patient's youth and consciousness were enough to overcome his abnormal vital signs. While the patient did experience mild tachypnea and tachycardia, he was ultimately not a very high-risk patient. In the third case, the patient's youth and consciousness could not compensate for the significant drop in blood pressure and elevated respiratory rate. The model identified 60 mmHg systolic blood pressure as a "red flag", which should indicate to a trauma team that this patient is a priority. In panel D, the patient's age and oxygen saturation were the key warning signs and the reason she was high-risk.

Fig. 3-5 SHAP feature importance metrics for 4 patients that were correctly predicted as survived or deceased. Output values (bold), expressed as log odds ratio of probability of survival to probability of deceased (i.e. $\log(\frac{p_{surv}}{1-p_{surv}})$), that are < 0 represent deceased patients (Cases A, C, D). Blue bars indicate that the feature value is increasing the probability of survival while red bars indicate that the feature is decreasing it.

We also computed the SHAP values for 8 cases where the model made incorrect predictions, as shown in Fig. 3-6 and Fig. 3-7. Notably, in all 8 cases, there was a single feature that dominated the model prediction (GCSTOT, Age, and SaO2) instead of a combination of features as in Fig. 3-5. Machine learning models are typically best at making predictions on unseen data that are as close to an interpolation of the training data as possible, and often fail when the unseen data is significantly different from the training data. One possible solution could be to explicitly model cross terms in the data to force the model to consider all feature-feature interactions. While the model is ideally learning the feature-feature interactions during the training process, sometimes explicit inclusion of these terms can improve model accuracy (although potentially at the expense of model interpretability).

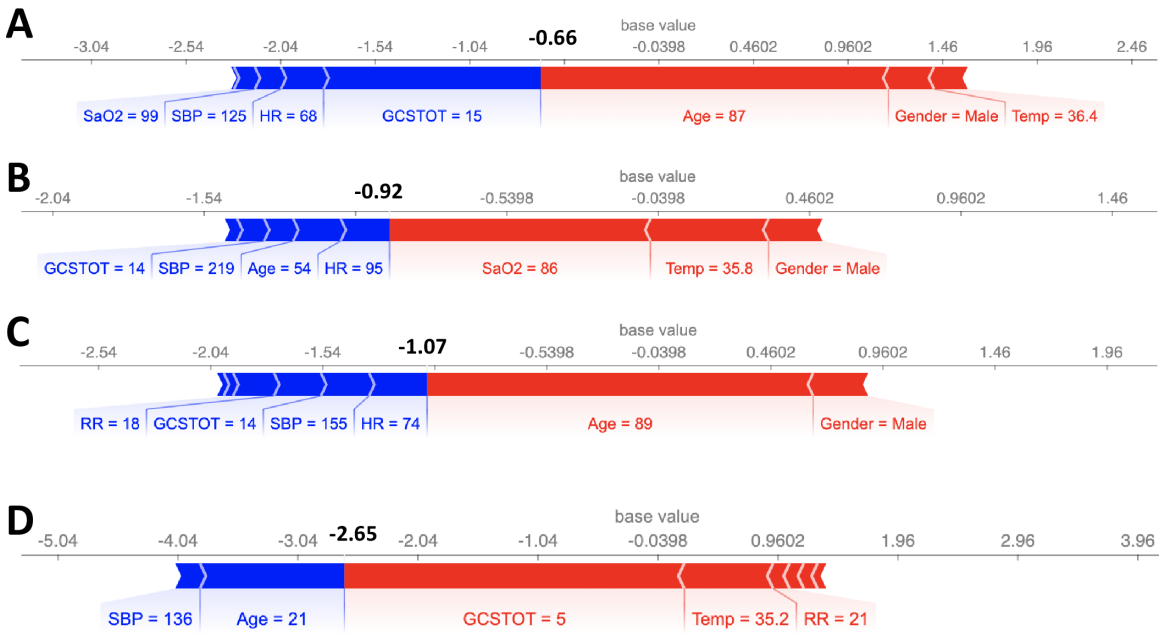

Fig. 3-6 SHAP feature importance metrics for 4 patients that were incorrectly predicted as deceased. Output values (bold), expressed as log odds ratio of probability of survival to probability of deceased (i.e. $\log(\frac{p_{surv}}{1-p_{surv}})$), that are < 0 represent deceased patients. Blue bars indicate that the feature value is increasing the probability of survival while red bars indicate that the feature is decreasing it. In all 4 cases, there was one feature that dominated the model prediction.

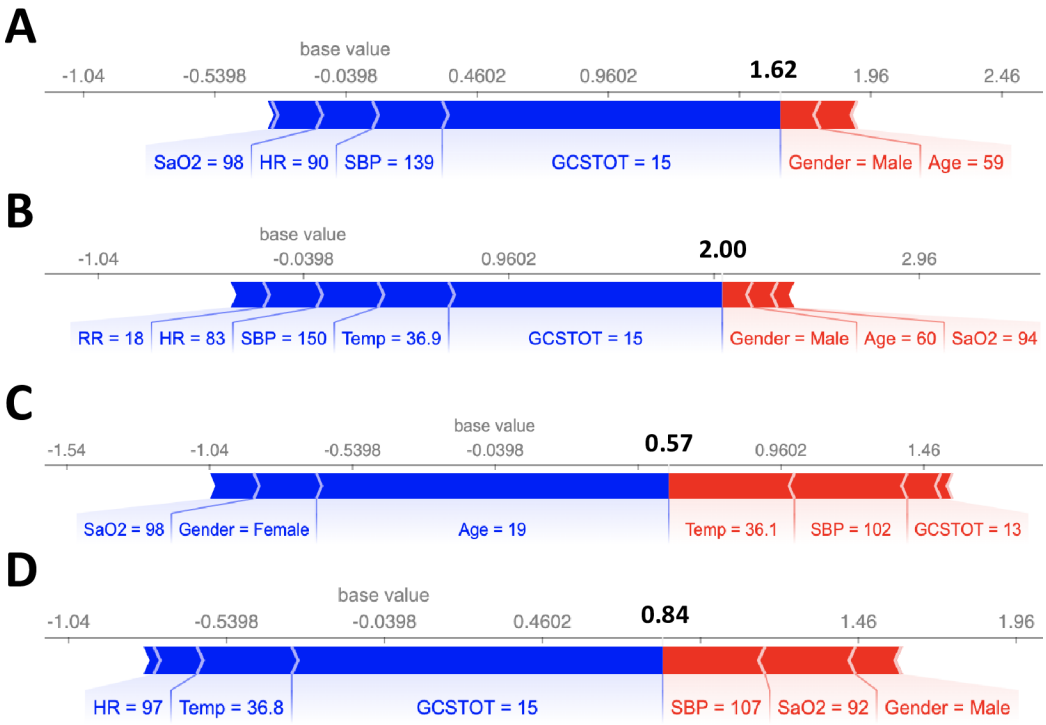

Fig. 3-7 SHAP feature importance metrics for 4 patients that were incorrectly predicted as survived. Similar to incorrectly predicting deceased cases, there was one feature that dominated the model prediction.

3.5 Discussion

The NTDB-trained gradient boosting model was trained with thousands of trauma patients from participating trauma centers around the country and was able to fit a robust decision boundary to the dataset. With only 8 features that can be measured upon a patient's ER admission, our model was able to provide an accurate metric for patient risk of death (AUC = 0.924, Fig. 3-2) even when death was rare. This high accuracy was further tested on a withheld dataset to further validate our claims of its high accuracy.

In a trauma setting, the usefulness of a model is not only limited by its accuracy but also by its interpretability – clinicians must understand how the model makes predictions in order to trust it. This has typically resulted in the use of linear models, but unfortunately, linear models are incapable of modeling complex decision boundaries - resulting in the loss of accuracy in exchange for interpretability. SHAP scores circumvent this problem by providing a robust method for quantitatively explaining a model's predictions. Using our model in conjunction with SHAP scores for the 8 features (Fig. 3-5) provides a detailed and quantitative view of each vital sign's contribution to risk. The method may serve several distinct uses. In a prioritization setting, where both time and nurse/surgeon availability are limited, the rapid generation of a hierarchy for patient treatment has value. The model can provide an objective ranking as to which patients should receive the most available resources and guide triage. Another use is to help explain those objective rankings with specific references to patient vital signs, potentially enhancing the prioritization.

Furthermore, they can be used to evaluate how actions taken to alter these variables may affect patient survival probability.

A limitation of this model is that it was trained based on the vital signs of patients upon admission. While the model was accurate, predicting the time-series evolution of the patient will requires dynamical training data. A natural extension would be to train a model that can predict patient-risk in real-time if time-series trauma patient data is available.

On the machine learning side, one limitation of our approach was the random undersampling procedure for balancing the number of *survived* patients with the number of *deceased* patients in the training set (124). It is possible that more informative survived patients were not included in the training set that could have led to an even more robust decision boundary (125). Undersampling methods that include *survived* examples based upon their distances to *deceased* patients in the 8-dimensional space could improve model predictability, as they can more accurately model the decision boundary near "hard-to-classify" cases (125). We also used the synthetic minority oversampling technique (SMOTE) to try to balance the training set, where artificial patient records from the *survived* class are generated from existing survived patient records, but it was ineffective in this instance and the accuracy of our model decreased significantly (126).

Although not the focus of this paper, we also note that the gradient boosting method exhibited a ROC-AUC that exceeded that of various neural networks and other machine learning models. Neural networks and tree-based models are two of the most commonly used classification models in the machine learning community with neural networks frequently outperforming tree-based models as well (127). While we extensively tuned the parameters to the neural network in hopes of attaining a higher accuracy, it was unable to eclipse our gradient boosting model.

The advantages of the present approach are: (1) only 8 features are needed, (2) all 8 features are readily available on admission, (3) the calculation is exceedingly fast, portable and accurate, (4) the relative risk of each feature is determined and graphically presentable as in Fig. 3-5 and 3-6, and (5) actual outcomes can be compared to the NTDB average performance on an individual basis. While features were chosen for inclusion based upon availability and importance, the accuracy of the model could be further improved by also including approximated inputs. For example, trauma surgeons generally also have an approximation for the injury severity score upon admission. If estimates for the severity of each injury is included into the model, the accuracy of the model was found to increase by ~2-3%. In future work, a goal will be to determine if the model predictions can be refined as a patient's vital signs evolve in time.

CHAPTER 4: PREDICTING RISK FOR TRAUMA PATIENTS USING STATIC AND DYNAMIC INFORMATION FROM THE MIMIC-III DATABASE

4.1 Abstract

Risk quantification algorithms in the ICU can provide (1) an early alert to the clinician that a patient is at extreme risk and (2) help manage limited resources efficiently or remotely. With electronic health records, large data sets allow the training of predictive models to quantify patient risk. A gradient boosting classifier was trained to predict high-risk and low-risk trauma patients, where patients were labeled high-risk if they died within the next 10 hours or within the last 10% of their ICU stay duration. The MIMIC-III database was filtered to extract 5,400 trauma patient records (526 non-survivors) each of which contained 5 static variables (age, gender, etc.) and 28 dynamic variables (e.g., vital signs and metabolic panel). Training data was also extracted from the dynamic variables using a 3-hour moving time window whereby each window was treated as a unique patient-time fragment. We extracted the mean, standard deviation, and skew from each of these 3-hour fragments and included them as inputs for training. Additionally, a survival metric upon admission was calculated for each patient using a previously developed National Trauma Data Bank (NTDB)-trained gradient booster model. The final model was able to distinguish between high-risk and low-risk patients to an accuracy of 92.9%, defined as the area under the receiver operator characteristic curve. Importantly, the dynamic survival probability plots for patients who die appear considerably different from those who survive, an example of reducing the high dimensionality of the patient record to a single trauma trajectory.

4.2 Introduction

Trauma is the leading cause of death in the United States for people over the age of 46 and the leading cause of overall expected years of life lost (60). Since modern intensive care units (ICU) monitor patients continuously, the data-rich environment can be used to predict mortality, time-dependent risk, and provide opportunities for data science and machine learning (128,129). Due to the high patient-to-patient variability, a data-driven approach is a reasonable way of predicting patient outcomes as patient-scale mechanistic models developed from first principles are highly challenging and likely injury-specific (70,110,111). Furthermore, time-series classification has already been successfully implemented in the field of medical diagnosis suggesting its potential utility in the context of trauma (130). The Medical Information Mart for Intensive Care (MIMIC-III) database is one of the first initiatives for not only the frequent collection of clinical patient data, but also the public dissemination of this de-identified data to be used by researchers around the world. This database is now the gold standard for publicly available time-stamped patient data, consisting of a very large patient population (> 40,000 patients) and time-stamped records of every clinical event.

To date, there has been considerable work aimed at predicting ICU patient outcomes. Alistair et al. predicted mortality to an area under the receiver operator characteristic curve (AUROC) of 92.4% using features extracted from the first 24 hour of a patient's stay in the ICU (131). Harutyunyan et al. predicted mortality within 24 hours to an AUROC of 91.1%, while simultaneously predicting average length of stay, an additional important variable for quantifying the efficacy of the ICU (132). In an earlier study, our group predicted mortality in the National Trauma Data Bank (NTDB) to an AUROC of 91.8%,

using only 8 static data points [age, gender, respiratory rate, heart rate, systolic blood pressure, Glasgow coma score, temperature, oxygen saturation] obtained upon admission into the hospital or ambulance, but not including data collected in the ICU (133). In addition to mortality analysis, length-of-stay prediction has been the focus of many machine learning groups as well, as it is a useful measure for managing hospital resources, improving outcomes, and increasing efficiency (134,135). Liu et al. published a detailed review on machine learning for trauma patients (108). There have also been physics-based models constructed to model trauma. Ursino et al., developed a system of ordinary differential equations to describe the circulatory system as a closed loop with feedback, which has been extended to simulate traumatic bleeding (7,110). While able to simulate blood loss patterns, these types of models are difficult to connect a specific injury to an outcome (20,68,70,136). Hirshberg et al., also developed a model to evaluate the impact of the transfusion of blood products on dilutional coagulopathy and found that resuscitation with more than 5 units of red blood cells would lead to coagulopathy (137).

In this paper, we use the MIMIC-III ICU database to predict risk of death in trauma patients and whether a patient's health will begin to rapidly decline (analogously, a rapid rise in risk). We pose this problem as a time-series classification problem where the input is a fixed-length window of patient properties (both dynamic and static) with a 1-hour step size. Each patient 3-hour window is regarded as a patient-time fragment that is used for training or evaluating a model. The goal of this work is to develop a model that can continuously assess and predict patient mortality probability (a metric for quantifying patient risk) as data becomes available.

4.3 Methods

4.3.1 Patient Dataset

The MIMIC-III dataset is publicly available and consists of more than 60,000 ICU admissions in 25 *.csv* files (Fig 4-1A). The patient dataset contains both static features (age, gender, etc.) and dynamic features (heart rate, blood pressure, etc.) and is suitable for the study of time-varying processes in trauma patients. We used an exclusion criterion consistent with the work of Alistair et al., where patients were excluded if they were neonatal or pediatric patients (age < 16), presented in the ICU for less than 4 hours, or had a do not resuscitate order (131). We also excluded patients with more than a single ICU stay per admission and filtered for patients who had external traumatic injury ICD-9 codes to ensure that we were gathering trauma patients; filtering criteria are listed in Fig. 4-1B. Following these exclusion and inclusion criteria, the dataset contained 5400 unique ICU visits (corresponding to 5400 unique patient records). Patient data was recorded at 1-hour time points after admission into the ICU.

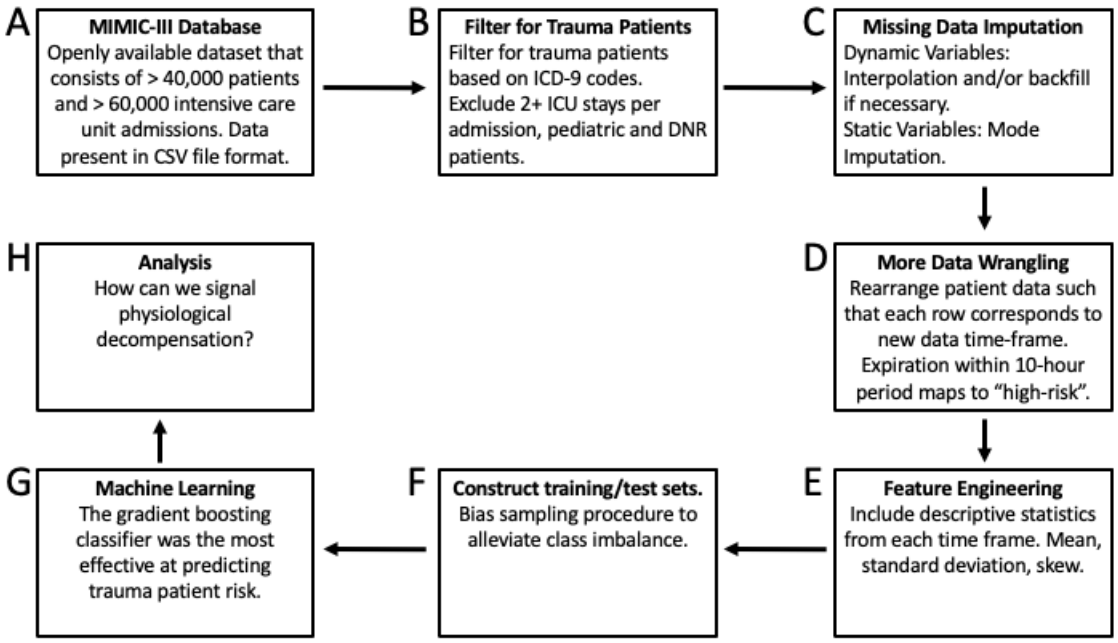

Fig. 4-1 Process flow diagram of the workflow for building a model to predict physiological decompensation. The data comes from the MIMIC-III database, an openly available dataset consisting of >40,000 patients, >60,000 intensive care unit admissions, and 25 .csv files. We filtered for trauma patients based on ICD-9 codes, and imputed missing data using mode imputation for static variables and interpolation for dynamic variables. We rearranged the data and posed it as a classification problem within a moving-window, where we tried to predict high-risk (death within 10-hours or death within the final 10% of the patient's total ICU stay duration). We extracted the mean, standard deviation, and skew for every dynamic variable. We constructed the training and test sets while biasing the sampling procedure to alleviate the class imbalance problem (the ratio of patients who survived to those who died was ~10:1). We then trained the gradient boosting classifier and analyzed whether it can be used to signal extreme risk of death.

4.3.2 Missing data

Missing data was handled in one of two ways. Mode imputation was used to impute the missing values and outlier values for all static variables used in the analysis (e.g., age, height, weight, BMI). For dynamic variables, we used linear interpolation method to populate the missing values. The vital signs of an exemplary patient are shown in **Fig. 4-2**. In some cases, the features varied greatly and displayed large fluctuations over the course of a patient's stay in the ICU (e.g., heart rate, respiratory rate, and systolic, diastolic, and mean blood pressure) and in other cases a variable may remain almost constant (e.g.,

hematocrit, hemoglobin, and Glasgow Coma Score). The high dimensionality of such data can become challenging even for an expert to rapidly interpret. Ideally, machine learning models are equipped to accommodate these high-dimensional patterns and use them to predict patient-risk.

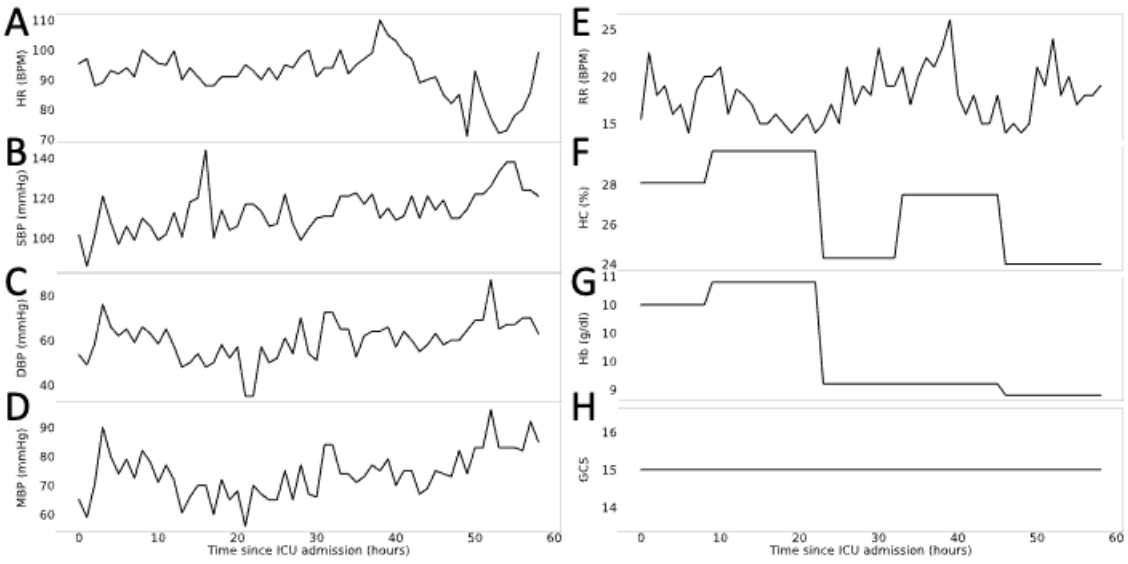

Fig. 4-2 The vital signs of a single patient's stay in the ICU.

4.3.3 Data Formatting

We posed this problem as a binary-classification problem where the data from the 3-previous time points was used to predict mortality over the following 10 hours. By posing the problem in this manner, the labels we were seeking to predict were effectively "high-risk" and "low-risk" (**Fig. 4-1D**). We further hypothesized that the most recent patient history was more predictive of patient-risk than the long-term patient history. Since we computed the descriptive statistics of each of the features, this would be akin to computing

these statistics with an exponential moving average and a small half-life (thus, more highly weighting the most recent data points).

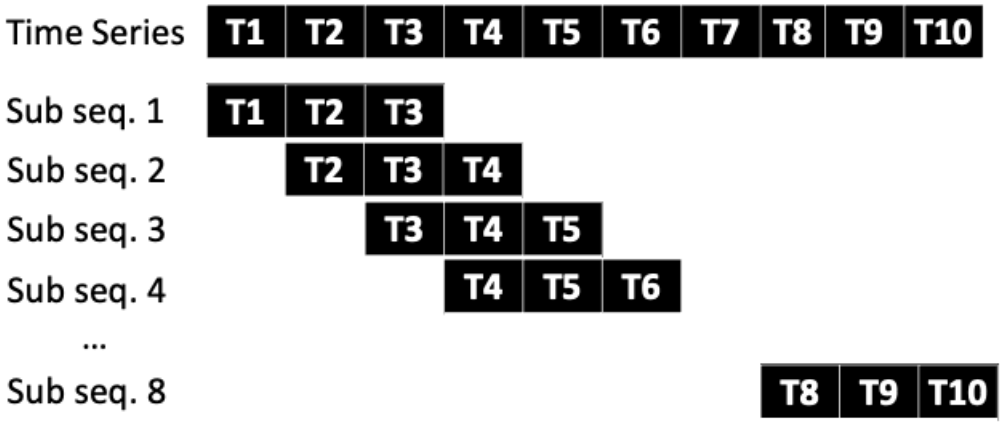

Fig. 4-3 Construction of the dataset from the raw data. Patient trajectories were divided into 3-hour window subsequences with a 1-hour step size.

4.3.4 Feature Selection

The dataset consisted of both static and dynamic variables. One of the most common treatments of dynamic analysis is to extract features based upon the entire time window. In this analysis, we performed a less common approach which is to divide the original patient vital sign evolution into multiple subsequences with a fixed step size and window length. This approach implicitly assumes that the short-term patient history is more significant to the outcome of the patient than the long-term patient history. For each trauma patient, we specified a 3-hour time window referred to as a *patient time fragment*. Within each time fragment, we extracted the mean, standard deviation, and skew for each of the dynamic variables, as shown in Fig. 4-1E.

Importantly, only vital sign and lab measurements from the basic metabolic panel were used and a complete list of features is shown in Table 4-1. This is consistent with the work of Alistair et al. who used similar features in their analysis (131). In addition to vital sign and lab measurement data, we also included the survival probability prediction of the model from our previous publication based only on time-equals-zero admission data (133). While this prior model was trained on static data primarily taken from trauma patients upon admission to the hospital, the inputs to this model (age, gender, temperature, GCS, SBP, O2SAT, HR, RR) are all present in this MIMIC-III dataset. Therefore, the survival probability predictions from the PLOS model were calculated and included as a feature for each patient at every time-point. We also included the static variables shown in the second column of Table 4-1, which were held constant across all patient time fragments. This analysis resulted in 89 features (5 static variables, and 3 features extracted from each of the 28 dynamic variables).

Table. 4-1 Features extracted from the dataset. Importantly, these extractions occurred over a 3-hour window of time length for each patient. A 1-hour step size was used to construct each patient fragment. The mean, standard deviation, and skew was included for each of the dynamic variables.

Dynamic Variables	Static Variables
Heart Rate	Sex
Systolic Blood Pressure	Age
Diastolic Blood Pressure	Height
Mean Blood Pressure	Weight
Respiratory Rate	BMI
Temperature	

Oxygen Saturation

Glucose levels

Glasgow Coma Score

Anion Gap

Albumin levels

Bicarbonate levels

Bilirubin levels

Calcium levels

Creatine levels

Chloride levels

Lactate levels

Platelet levels

Potassium levels

Sodium levels

Prothrombin Time

International Normalized Ratio

Hematocrit

Hemoglobin

Blood Urea Nitrogen

White Blood Cell count

Endotracheal tube requirement flag

PLOS-NTDB Model Prediction (133)

4.3.5 Class Imbalance

Of the 5400 trauma patients in the MIMIC-III database, 526 of them died. While not an enormous class imbalance, the dataset consisted of 158,108 patient windows of which only 5,615 mapped to high-risk patients. If one were to randomly assign patients to either the training set or the test set without accounting for this imbalance, the model will simply learn to label each patient as low-risk (the majority class) as this will maximize its accuracy (although it would not have learned anything meaningful). To alleviate this class imbalance, we undersampled from the population that survived to develop the training set, as described in **Fig. 4-1F** (124). Patients who ultimately died were assigned a higher probability of being placed in the training set than in the test set. Importantly, all of the patient windows corresponding to a specific patient were present in either the training set or test set, an important point to ensure that we are not fitting our model to data present in the test set, a process known as data leakage.

4.3.6 Machine Learning Modeling

A gradient boosting classifier as trained to predict high-risk and low-risk patient windows, the penultimate step in the process flow diagram and shown in **Fig. 4-1G** (112). The algorithm works by training 300 weak learners, typically short decision trees, on the dataset in a stage-wise manner so that the errors made by the early weak learners are corrected by the latter ones. Gradient boosting receives high recognition in the literature for its effectiveness in classification on tabular data (138,139). We also trained other common machine learning models to the dataset (e.g., support vector machine, logistic regression, and gaussian naïve Bayes) but the gradient boosting classifier was found to outperform all

other models. With the model trained, we were left to interpret the results as represented in **Fig. 4-1H**.

4.4 Results

The accuracy of the model is expressed as the area under the receiver operator characteristic curve (AUROC), which is the probability of correctly distinguishing between a high-risk patient time fragment and a low-risk patient time fragment. Using this as the metric for the model, we achieved an accuracy of 92.9%. We also compared this accuracy with other machine learning models and found that it outperformed the support vector machine classifier, the logistic regression classifier, and the Gaussian Naïve Bayes classifier (Fig. 4).

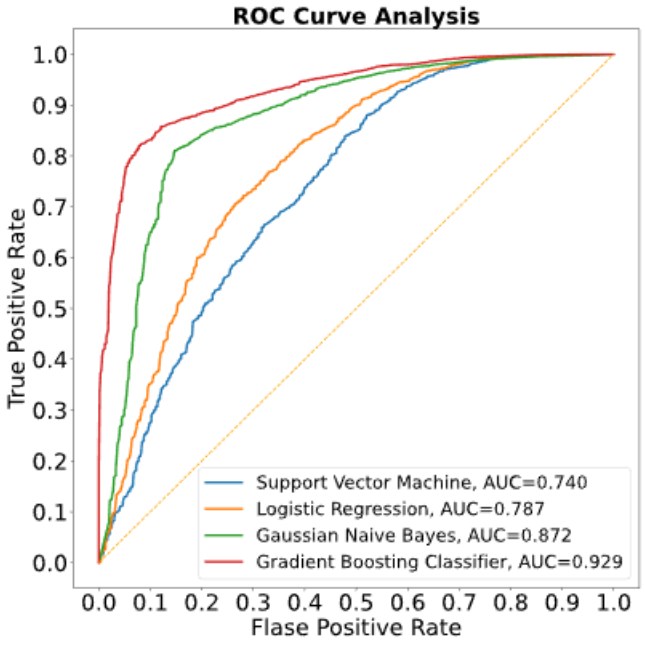

Fig. 4-4 The ROC Curve for every machine learning model that we trained. The gradient boosting classifier is the most accurate and the one used in the subsequent analysis.

We plotted the probability of survival against the time prior to expiration or discharge for patients who died (**Fig. 4-5**) and those who survived (**Fig. 4-6**). The survival probability plots of patients who died exhibited either a sudden drop in survival probability in the hours prior to death or had survival probabilities weakly fluctuating at very low survival

probability values (e.g., **Fig. 4-5E** and **Fig. 4-5F**). In the patients who survived, we generally observed the opposite behavior. Survival probabilities would either rise, remain the same, or experience minor drops that were not indicative of extreme risk of death.

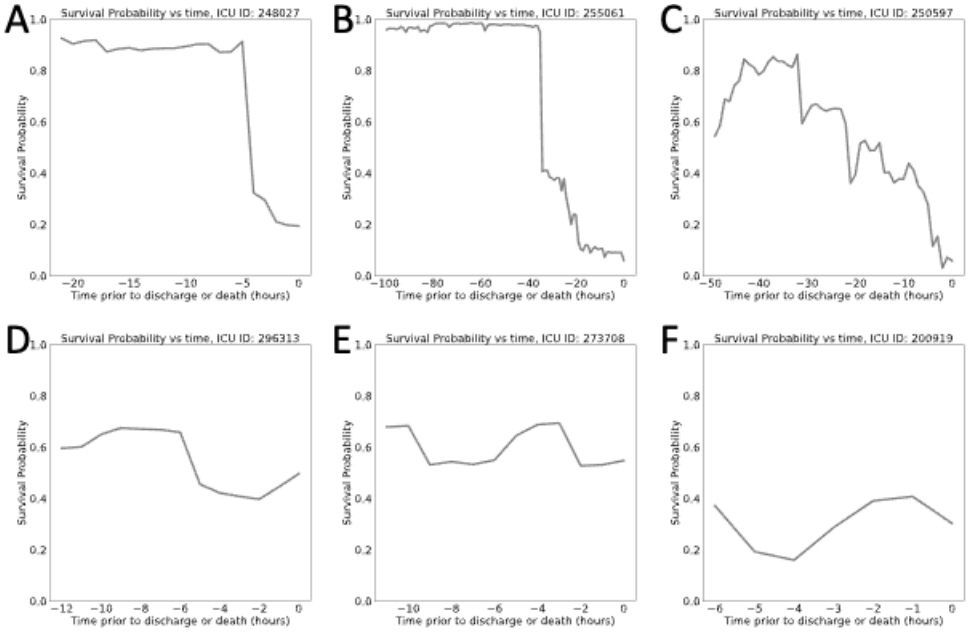

Fig. 4-5 Survival probability plots for a subset of patients who ultimately died. Notice that many of these patients experienced a sudden dip in survival probability prior to death, except for one displayed in panel F, where the probability of survival of this patient was consistently low (<0.4 for all time points).

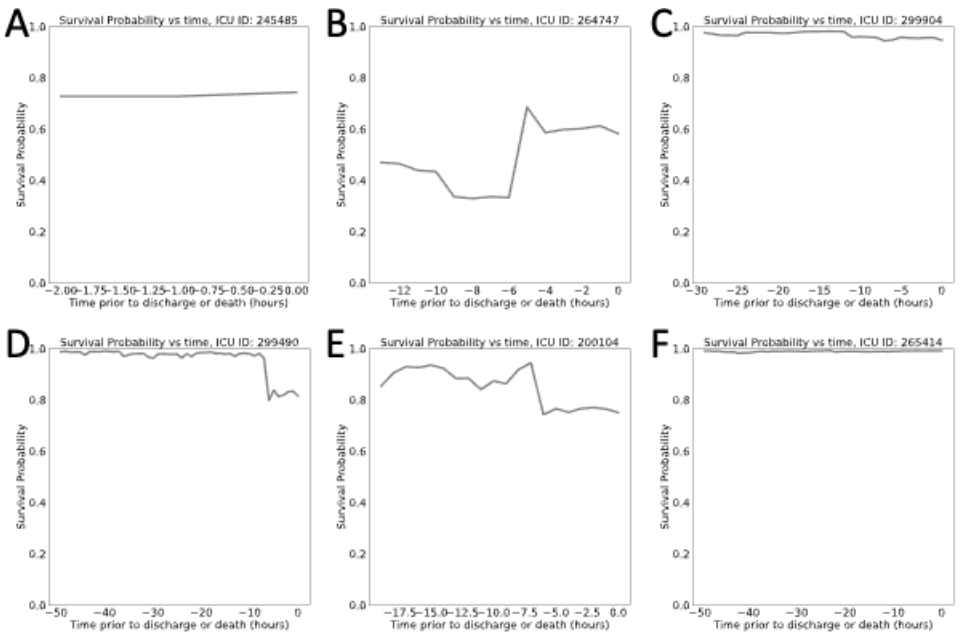

Fig. 4-6 Survival probability plots for a subset of patients who survived. Note that probability of survival remains the same or increases, but rarely displayed a sudden, dramatic drop.

4.5 Discussion

The gradient boosting classifier was able to accurately predict risk in the trauma patients present in the MIMIC-III database with dynamic (vital signs, basic metabolic panel values) and static (age, gender, etc.) values. This machine learning methodology naturally raises certain questions as to how the model should be implemented and interpreted mechanistically. If an absolute, and arbitrary, threshold is used to indicate extreme risk of death, it would not be accurate for detecting this extreme risk in severe cases. An outlier detection method for detecting sudden drops in survival probabilities may be more appropriate, as it will be able to trigger a response from ICU team. As it stands, the relatively small number of deceased patients make it difficult to determine its effectiveness, but as more data becomes available, this should be the focus of future work.

One of the key assumptions of this analysis was that the time-prior to death or discharge from the ICU was specified prior to training, a variable we will refer to as lead-time. We performed a sensitivity analysis on this variable, as it represents a balance between predictive power (high AUROC) and value in a clinical setting (the greater the lead-time, the more useful the model is) which is shown in Fig. 4-7. Based on the concavity of plot and apparent inflexion point around 10-hours, this value seems to be a fair compromise between these two factors.

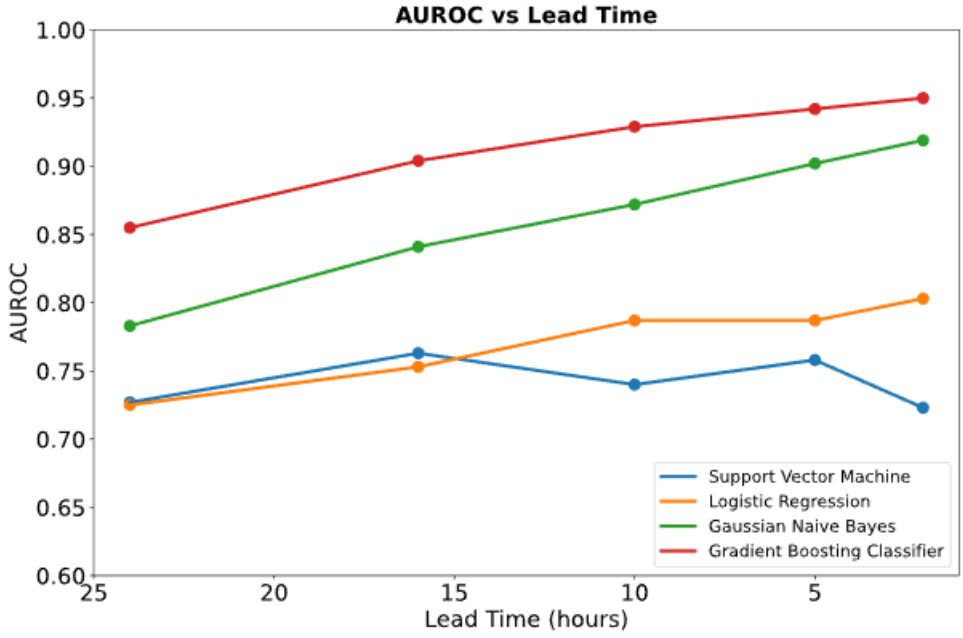

Fig. 4-7 A sensitivity analysis of the lead time for each of the 4 machine-learning models. We can see that a 10-hour lead-time achieves a high accuracy and identifies risk accurately by 10-hours ahead of time, a considerable amount of time. The gradient boosting classifier also outperformed each of the other 3 models regardless of the label start time.

There are other limitations of this model as well. First, all of the data used in this analysis are from the same hospital making it unclear if it is predictive of all hospitals. In theory, a similar approach can be taken if data is unified from participating trauma centers but to our

knowledge this has not occurred yet. The National Trauma Data Bank (NTDB) consists of trauma patient data but mostly contains static data (113). Second, our analysis was only performed on trauma patients suggesting that it may not generalize to other disease states. Furthermore, while our methodology resulted in 158,108 time points, this only represented 5,400 trauma patients, a relatively small number. As is usually the case in problems with limited data available, more data could dramatically improve accuracy and garner more insights. We hope that this paper, as well as the works of groups, can help elucidate the need for publicly available, de-identified, patient data for in-depth analysis.

Another limitation of the present model is its interpretability. While gradient boosting classifiers tend to perform very well on tabular datasets, they often lack the interpretability of simpler models such as the logistic regression classifier and clinicians must have an understanding of how the model works in order to trust it. Tools such as the Local Interpretable Model-Agnostic Explanations method (LIME) or Shapley Additive Explanations (SHAP) value metrics are used to interpret these models, but their reliability is an active area of research (140). Interpretability is a key component of a machine learning models in most settings, but especially healthcare since it may often have the direst consequences.

Clearly, publicly available EHR spell out data presents an opportunity for patient outcome improvements. In this work, we demonstrated the utility of gradient booster classification in handling static and dynamic data. Additionally, we demonstrated the utility of the patient time fragment as a useful protocol for extracting information from time series with the goal of training machine learning algorithms. Importantly, the dynamic survival probability

plots for patients who die appear to be considerably different from those who survive, an example of the benefit of reducing the high dimensionality of the patient record to a single trauma trajectory.

CHAPTER 5: FUTURE WORK

5.1 Multiscale Modeling

The multiscale model of a trauma patient that we developed offers the potential to optimize treatment options and quantify difficult to observe mechanisms important to patient outcome. Unfortunately, there are important processes that lack suitable biomarkers or measurable attributes, despite their importance. For example, mean arterial pressure is used as a metric for blood loss since cumulative and instantaneous blood loss are not known quantities in the trauma patient. Patient hydration status is important for quantifying the influence of transcapillary fluid shifts in attenuating hypovolemia, although this is also typically unknown. The pre-trauma pharmacology of a patient is important but typically unknown, particularly antiplatelet and anticoagulant agents or drugs of abuse. The injury distribution of the patient is required for the model, a factor that is typically unknown in a trauma setting. While the model can provide quantitative insights into patient evolution, it is currently difficult to implement in a practical trauma patient setting.

Platelet and endothelial dysfunction, anticoagulation, hyperfibrinolysis have all been implicated during major trauma, an effect known as trauma-induced coagulopathy (TIC) (93). The simulations in this model were relatively short (< 2 hours) and the timescale for TIC is on the order of many hours. On the other hand, longer simulations would require careful consideration of TIC where both variable hematocrit and impaired platelet

aggregation would need to be included. Trauma modeling efforts on the order of days must take this phenomenon into account.

The BVN also makes several assumptions about the geometry of the vascular network for simplicity. The first assumption is parabolic flow through rigid, cylindrical, blood vessels. While this is generally a fair assumption, arteries and arterioles may be quite compliant and easily deformable with ~40% changes in diameter and non-circular, non-constant cross-sectional shape across the entire length of the blood vessel. This assumption leads to inaccuracies in vessel resistance calculations, in general underestimating them. However, while the resistance through an individual blood vessel is uncertain, the overall resistance of the BVN is more accurately calculated (79). Since vessel severs were made a minimum of 10 generations from the root vessel, an accurate resistance for the bleeding BVN is still computed for our purposes. However, if a modeler is interested in simulating blood loss from an individual blood cell rather than a network, this must be explicitly modeled.

Trauma presents complex and rapidly evolving scenarios for clinical decision making. As a patient bleeds, the individual's life may be at extreme risk if their systemic blood function changes in a manner that is unable to stop further bleeding. The overall goal is to achieve multiscale simulation of the trauma patient by accounting for changes in the systemic circulation and the traumatized blood and tissue so as to better stratify patient bleeding (or clotting) risks, prioritize improved biomarkers of risk, and potentially identify new opportunities for safer treatments. Although at an early stage of development, improved multiscale vessel and blood-tissue models will be broadly useful to other clinical situations

of: surgical bleeding, sepsis, consumptive coagulopathies, deep vein thrombosis, acute lung injury, and hemophilic bleeding.

5.2 Machine Learning

In the field of machine learning, advanced algorithms are freely available and computing power is at an all-time high. The bigger limit at this point is data availability, as de-identified trauma-patient data is not publicly available. All of the data used in this analysis comes from the same hospital making it unclear if it is predictive of all hospitals. In theory, a similar approach can be taken if data is unified from participating trauma centers but to our knowledge this has not occurred yet. The National Trauma Data Bank (NTDB) consists of trauma patient data but mostly contains static data (113).

We demonstrated that our machine-learning model can make accurate predictions for patient-risk but forecasting patient-evolution is not present which may be tremendously useful in predicting appropriate intervention time-points. We can predict whether a patient will decompensate but predicting the evolution of this patient in terms of measurable quantities (e.g., vital signs) might be the focus of future work.

Appendix A: Multiscale model supplemental figures

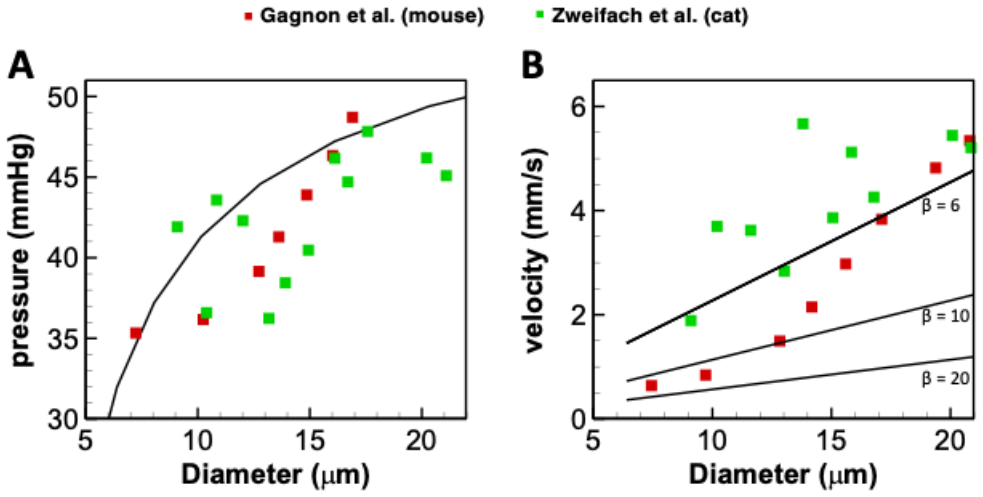

Fig. A-1 Model validation prior to Bleeding. Comparison of multiscale model with in vivo pressure (**A**) and velocity (**B**) measurements in the mouse (81) and in the cat (80).

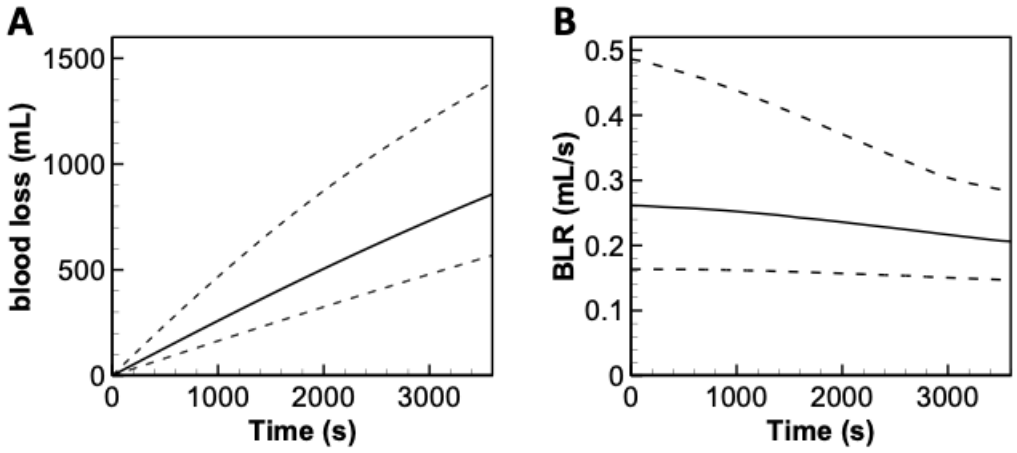

Fig. A-2 Effect of branching exponent variability. To further examine the influence of the branching parameter, k, 1000 simulations were run with k randomly chosen from a uniform distribution between 2 and 3 at each generation. The cumulative blood loss (**A**) and the blood loss rates (**B**) include dashed lines representing the most extreme results and the black line represents the most common result. Small deviations in this geometric parameter can lead to ~3-fold change in these curves.

Appendix B: PLoS NTDB model supplemental figures

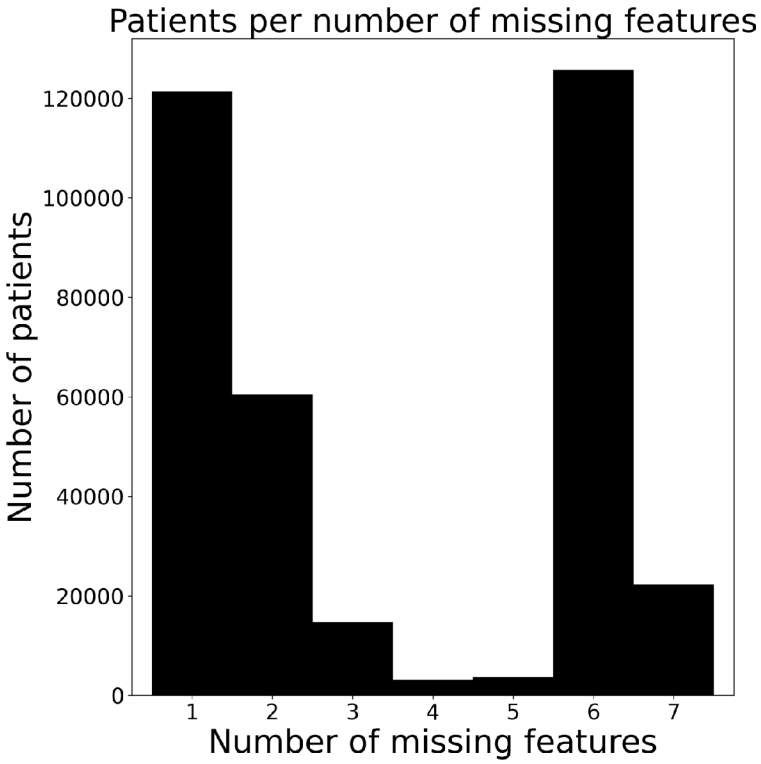

Fig. B-1 A distribution of the number of patients per number of missing features. The distribution is bimodal, suggesting that including patients with a maximum of 2 missing features is the appropriate threshold for inclusion.

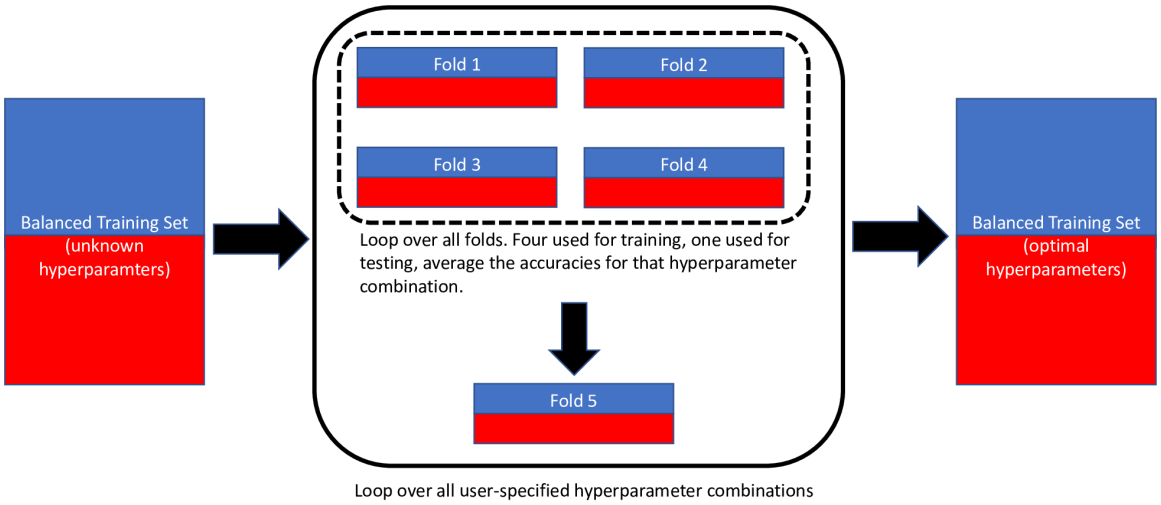

Fig. B-2 The 5-fold grid-search cross validation method for selecting the approximately optimal hyperparameters. Importantly, the test set was withheld during the grid-search cross validation process allowing it to remain a fair metric for evaluating performance on new data.

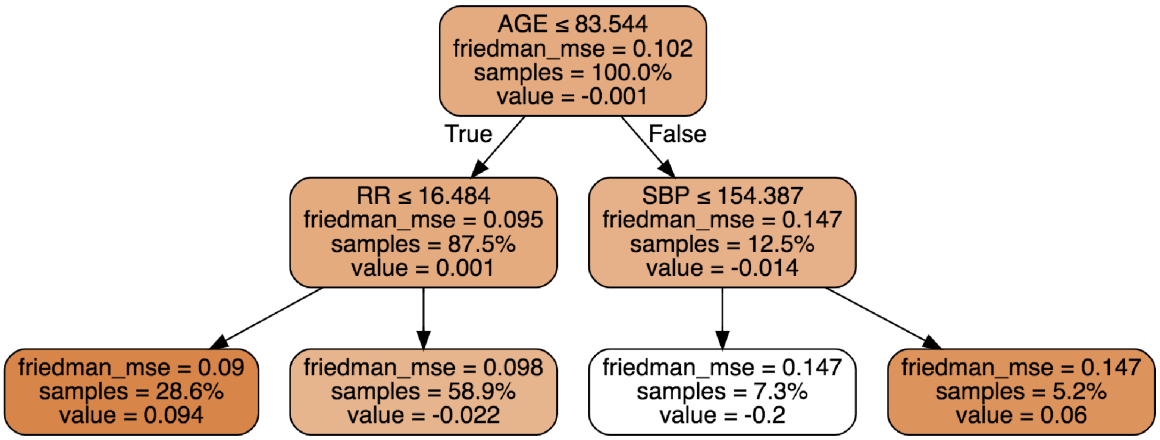

Fig. B-3 A single weak learner randomly chosen from the trained gradient boosting ensemble of weak learners. Variable thresholds, Friedman mean squared errors (112), percentage of training samples passed through each node, and log odds ratios are all present.

Table. B-1 Performance comparison of various supervised machine learning models.

Model	ROC-AUC
Gradient Boosting Classifier	0.918
Neural Network	0.910
Decision Tree Classifier	0.817
Adaboost Classifier	0.907
Random Forest	0.896

BIBLIOGRAPHY

1. Giles AR, Nesheim ME, Herring SW, Hoogendoorn H, Stump DC, Heldebrant CM. The Fibrinolytic Potential of the Normal Primate Following the Generation of Thrombin in Vivo. Thromb Haemost. 1990;63(3):476–81.

2. Kutcher ME, Redick BJ, McCreery RC, Crane IM, Greenberg MD, Cachola LM, et al. Characterization of platelet dysfunction after trauma. J Trauma Acute Care Surg. 2012;73(1):13–9.

3. Ostrowski SR, Sørensen AM, Windeløv NA, Perner A, Welling KL, Wanscher M, et al. High levels of soluble VEGF receptor 1 early after trauma are associated with shock, sympathoadrenal activation, glycocalyx degradation and inflammation in severely injured patients: a prospective study. Scand J Trauma Resusc Emerg Med [Internet]. 2012;20(27). Available from: http://www.sjtrem.com/content/20/1/27

4. Marumo M, Suehiro A, Kakishita E, Groschner K, Wakabayashi I. Extracellular pH affects platelet aggregation associated with modulation of store-operated Ca2+ entry. Thromb Res. 2001;104(5):353–60.

5. Dirkmann D, Hanke AA, Görlinger K, Peters J. Hypothermia and acidosis synergistically impair coagulation in human whole blood. Anesth Analg. 2008;106(6):1627–32.

6. Reisner AT, Heldt T. A computational model of hemorrhage and dehydration

suggests a pathophysiological mechanism: Starling-mediated protein trapping. Am J Physiol Heart Circ Physiol [Internet]. 2013;304(4):H620-31. Available from: http://www.ncbi.nlm.nih.gov/pubmed/23203962

7. Ursino M. Interaction between carotid baroregulation and the pulsating heart: A mathematical model. Am J Physiol - Hear Circ Physiol. 1998;275(5 44-5):1733–47.

8. Llompart-Pou JA, Raurich JM, Pérez-Bárcena J, Barceló A, Ibáñez J, Ayestarán JI. Acute hypothalamic-pituitary-adrenal response in traumatic brain injury with and without extracerebral trauma. Neurocrit Care. 2008;9(2):230–6.

9. Hallow KM, Lo A, Beh J, Rodrigo M, Ermakov S, Friedman S, et al. A model-based approach to investigating the pathophysiological mechanisms of hypertension and response to antihypertensive therapies: Extending the Guyton model. Am J Physiol - Regul Integr Comp Physiol. 2014;306(9):647–62.

10. Westerhof N, Lankhaar JW, Westerhof BE. The arterial windkessel. Med Biol Eng Comput. 2009;47(2):131–41.

11. Guyton AC, Coleman TG, Granger HJ. Circulation: overall regulation. Anu Rev Physioal Rev Physio. 1972;

12. Osborn JW, Averina VA, D FG. Current computational models do not reveal the importance of the nervous system in long-term control of arterial pressure. Exp Physiol. 2009;94(4):389–96.

13. Magosso E, Ursino M. A mathematical model of CO2 effect on cardiovascular regulation. Am J Physiol - Hear Circ Physiol. 2001;281:2036–52.

14. Ursino M, Magosso E. Acute cardiovascular response to isocapnic hypoxia. I. A mathematical model. Am J Physiol Heart Circ Physiol. 2000;279:H149–65.

15. Ursino M, Magosso E. Acute cardiovascular response to isocapnic hypoxia. II. Model validation. Am J Physiol Heart Circ Physiol. 2000;279(1):H166–75.

16. Žáček M, Krause E. Numerical simulation of the blood flow in the human cardiovascular system. J Biomech. 1996;29(1):13–20.

17. Díaz-Zuccarini V, LeFèvre J. An energetically coherent lumped parameter model of the left ventricle specially developed for educational purposes. Comput Biol Med. 2007;37(6):774–84.

18. Yaku H, Goto Y, Futaki S, Ohgoshi Y, Kawaguchi O, Suga H. Multicompartment model for mechanics and energetics of fibrillating ventricle. Am J Physiol. 1991;260:H292–9.

19. Lu K, Clark J, Ghorbel F, Ware D, Bidani A. A human cardiopulmonary system model applied to the analysis of the Valsalva maneuver. Am J Physiol - Hear Circ Physiol. 2001;281(6):H2661–79.

20. Neal ML, Bassingthwaighte JB. Subject-specific Model Estimation of Cardiac Output and Blood Volume During Hemorrhage. Cardiovasc Eng. 2013;7(3):97–120.

21. Sterling S, Jones A, Coleman T, Summers R. Theoretical Analysis of the Relative Impact of Obesity on Hemodynamic Stability During Acute Hemorrhagic Shock. Arch Trauma Res. 2015;4(3).

22. Hirshberg A, Dugas M, Banez EI, Scott BG, Wall MJ, Mattox KL. Minimizing dilutional coagulopathy in exsanguinating hemorrhage: a computer simulation. J Trauma Inj Infect Crit Care [Internet]. 2003;54(3):454–63. Available from: http://eutils.ncbi.nlm.nih.gov/entrez/eutils/elink.fcgi?dbfrom=pubmed&id=12634523&retmode=ref&cmd=prlinks%5Cnpapers3://publication/doi/10.1097/01.TA.0000053245.08642.1F

23. Lewis F. Prehospital intravenous fluid therapy: physiologic computer modelling. J Trauma. 1986;26(9):804–11.

24. Horsfield K, Woldenberg M. Diameters and cross-sectional areas of branches in the human pulmonary arterial tree. Anat Rec. 1989;223(3):245–51.

25. Hutchins G, Miner M, Boitnott J. Vessel caliber and branch-angle of human coronary artery branch-points. Circ Res. 1976;38(6):572–6.

26. Wang S, Yu B. Study of the effect of capillary pressure on the permeability of porous media embedded with a fractal-like tree network. Int J Multiph Flow. 2011;37(5):507–13.

27. Yang J, Yongtian W. Design of vascular networks : A mathematical model approach. 2013;(2012).

28. Yang J, Pak YE, Lee TR. Predicting bifurcation angle effect on blood flow in the microvasculature. Microvasc Res. 2016;108:22–8.

29. Razavi MS, Shirani E. Development of a general method for designing microvascular networks using distribution of wall shear stress. J Biomech. 2013;46(13):2303–9.

30. Goldman D, Aleksander SP. A computational study of the effect of capillary network anastomoses and tortuosity on oxygen transport. J Theor Biol. 2000;206(2):181–94.

31. Westerhof N, Bosman F, De Vries C, Noordergraaf A. Analog studies of the human systemic arterial tree. J Biomech. 1969;2(2):121–43.

32. Pontrelli G, Rossoni E. Numerical modelling of the pressure wave propagation in the arterial flow. Int J Numer methods fluids. 2003;43(6–7):651–71.

33. Reymond P, Merenda F, Perren F, Rufenacht D, Stergiopulos N. Validation of a one-dimensional model of the systemic arterial tree. Am J Physiol - Hear Circ Physiol. 2009;297(1):H208–22.

34. Surovtsova I. Effects of compliance mismatch on blood flow in an artery with endovascular prosthesis. J Biomech. 2005;38(10):2078–86.

35. Pontrelli G. A multiscale approach for modelling wave propagation in an arterial segment. Comput Methods Biomech Biomed Engin. 2004;7(2):79–89.

36. Migliavacca F, Balossino R, Pennati G, Dubini G, Hsia T., de Leval MR, et al.

Multiscale modelling in biofluidynamics: application to reconstructive paediatric cardiac surgery. J Biomech. 2006;39(6):1010–20.

37. Monkovic DD, Tracy PB. Activation of human factor V by factor Xa and thrombin. Biochemistry. 1990;29(5):1118–28.

38. Diamond SL. Systems analysis of thrombus formation. Circ Res. 2016;118(9):1348–62.

39. Flamm MH, Diamond SL. Multiscale systems biology and physics of thrombosis under flow. Ann Biomed Eng. 2012;40(11):2355–64.

40. Fogelson AL, Neeves KB. Fluid mechanics of blood clot formation. Annu Rev Fluid Mech. 2015;47:377–403.

41. Brummel-Ziedeins KE, Everse SJ, Mann KG, Orfeo T. Modeling thrombin generation: plasma composition based approach. J Thromb Thrombolysis. 2014;37(1):32–44.

42. Shibeko AM, Panteleev MA. Untangling the complexity of blood coagulation network: use of computational modelling in pharmacology and diagnostics. Brief Bioinform. 2016;17(3):429–39.

43. Brown D, Namas RA, Almahmound K, Zaaqoq A, Sarkar J, Barclay D, et al. Trauma in silico: Individual-specific mathematical models and virtual clinical populations. Sci Transl Med. 2015;7(285):285ra61-285ra61.

44. Hockin MF, Jones KC, Everse SJ, Mann KG. A model for the stochiometric

regulation of blood coagulation. J Biol Chem. 2002;277(21):18322–33.

45. Danforth CM, Orgeo T, Mann KG, Brummel-Ziedeins KE, Everse SJ. The impact of uncertainty in a blood coagulation model. Math Med Biol a J IMA. 2009;26(4):323–36.

46. Chatterjee MS, Denney WS, Jing J, Diamond SL. Systems biology of coagulation initiation: kinetics of thrombin generation in resting and activated human blood. PLoS Comput Biol. 2010;6(9).

47. Zhu S, Lu Y, Sinno T, Diamond SL. Dynamics of thrombin generation and flux from clots during whole human blood flow over collagen/tissue factor surfaces. J Biol Chem. 2016;291(44):23027–35.

48. Bungay SD, Gentry PA, Gentry RD. A mathematical model of liped-mediated thrombin generation. Math Med Biol. 2003;20(1):105–29.

49. Butenas S, van't Veer C, Mann K. "Normal" Thrombin Generation. Blood, J Am Soc Hematol. 1999;94(7):2169–78.

50. Purvis JE, Chatterjee MS, Brass LF, Diamond SL. A molecular signaling model of platelet phosphoinositide and calcium regulation during homeostasis and P2Y1 activation. Blood, J Am Soc Hematol. 2008;112(10):4069–79.

51. Lenoci L, Duvernay M, Satchell S, DiBenedetto E, Hamm HE. Mathematical model of PAR1-mediated activation of human platelets. Mol Biosyst. 2011;7(4):1129–37.

52. Chatterjee MS, Purvis JE, Brass LF, Diamond SL. Pairwise agonist scanning predicts cellular signaling responses to combinatorial stimuli. Nat Biotechnol. 2010;28(7):727–32.

53. Kuharsky AL, Fogelson A. Surface-mediated control of blood coagulation: the role of binding site densities and platelet deposition. Biophys J. 2001;80(3):1050–74.

54. Leiderman K, Fogelson A. Grow with the flow : a spatial – temporal model of platelet deposition and blood coagulation under flow. 2011;

55. Okorie UM, Denney WS, Chatterjee MS, Neeves KB, Diamond SL. Determination of surface tissue factor thresholds that trigger coagulation at venous and arterial shear rates: amplification of 100 fM circulating tissue factor requires flow. Blood. 2008;111(7):3507–13.

56. Stalker TJ, Traxler E a, Wu J, Wannemacher KM, Cermignano SL, Voronov R, et al. Hierarchical organization in the hemostatic response and its relationship to the platelet signaling network. Blood [Internet]. 2013;121(10):1875–86. Available from: http://www.ncbi.nlm.nih.gov/pubmed/23303817

57. Xu Z, Chen N, Kamocka MM, Rosen ED, Alber M. A multiscale model of thrombus development. 2008;(October 2007):705–22.

58. Filipovic N, Kojic M, Tsuda A. Modelling thrombosis using dissipative particle dynamics method. Philos Trans R Soc A Math Phys Eng Sci. 2008;366(1879):3265–79.

59. Lu Y, Lee MY, Zhu S, Sinno T, Diamond SL. Multiscale simulation of thrombus growth and vessel occlusion triggered by collagen / tissue factor using a data-driven model of combinatorial platelet signalling. 2016;1:1–24.

60. Rhee P, Joseph B, Pandit V, Aziz H, Vercruysse G, Kulvatunyou N, et al. Increasing trauma deaths in the United States. Ann Surg. 2014;260(1):13–21.

61. Chang R, Cardenas JC, Wade CE, Holcomb JB. Review Article Advances in the understanding of trauma-induced coagulopathy. Blood. 2016;128(8):1043–50.

62. Brohi K, Cohen MJ, Davenport RA. Acute coagulopathy of trauma : mechanism , identification and effect. Curr Opin Crit Care. 2007;13(3):680–5.

63. Yanagida Y, Gando S, Sawamura A. Normal prothrombinase activity, increased systemic thrombin activity, and lower antithrombin levels in patients with disseminated intravascular coagulation at an early phase of trauma: Comparison with acute coagulopathy of trauma-shock. Surgery [Internet]. 2013;154(1):48–57. Available from: http://dx.doi.org/10.1016/j.surg.2013.02.004

64. Cap A, Hunt B. Acute traumatic coagulopathy. Curr Opin Crit Care. 2014;20(6):638–45.

65. Blanco PJ, Watanabe SM, Aur M, Passos RF, Lemos PA, Feij A. An Anatomically Detailed Arterial Network Model for One-Dimensional Computational Hemodynamics. 2015;62(2):736–53.

66. Hallow KM, Lo A, Beh J, Rodrigo M, Ermakov S, Friedman S, et al. A model-

based approach to investigating the pathophysiological mechanisms of hypertension and response to antihypertensive therapies: extending the Guyton model. Am J Physiol Regul Integr Comp Physiol [Internet]. 2014;306(9):R647-62. Available from: http://www.ncbi.nlm.nih.gov/pubmed/24500431

67. Ursino M. Interaction between carotid baroregulation and the pulsating heart : a mathematical model. 1998;1733–47.

68. Canuto D, Eldredge JD, Benharash P, Dutson EP. A regulated multiscale closed-loop cardiovascular model , with applications to hemorrhage and hypertension. Int J Numer Meth Biomed Engng. 2018;34(September 2017):1–25.

69. Ittal NM, Hou YZ, Ng SU, Inares CL, Olloi SM, Assab GSK. A Computer Reconstruction of the Entire Coronary Arterial Tree Based on Detailed Morphometric Data. 2005;33(8):1015–26.

70. Reisner AT, Heldt T. A computational model of hemorrhage and dehydration suggests a pathophysiological mechanism: Starling-mediated protein trapping. AJP Hear Circ Physiol [Internet]. 2013;304(4):H620–31. Available from: http://ajpheart.physiology.org/cgi/doi/10.1152/ajpheart.00621.2012

71. Sterling SA, Jones AE, Coleman TG, Summers RL. Theoretical Analysis of the Relative Impact of Obesity on Hemodynamic Stability During Acute Hemorrhagic Shock. 2015;4(3).

72. Colace T V, Muthard RW, Diamond SL. Cell Biology / Signaling Role of

Thrombin With and Without Fibrin. 2012;1466–76.

73. Colace T V., Diamond SL. Direct observation of von Willebrand factor elongation and fiber formation on collagen during acute whole blood exposure to pathological flow. Arter Thromb Vasc Biol. 2013;33(1):105–13.

74. Herbig BA, Diamond SL. Pathological VWF fibers resist tPA and ADAMTS13 while promoting the contact pathway and shear-induced platelet activation. 2016;13(9):1699–708.

75. Cheng L, Ivanova O, Fan H, Khoo MCK. An integrative model of respiratory and cardiovascular control in sleep-disordered breathing. Respir Physiol Neurobiol [Internet]. 2010;174(1–2):4–28. Available from: http://dx.doi.org/10.1016/j.resp.2010.06.001

76. Nadler S, Hidalgo J, Bloch T. Prediction of blood volume in normal human adults. Surgery. 1962;51:224–32.

77. Murray CD. The physiological principle of minimum work applied to the angle of branching of arteries. Proc Natl Acad Sci. 1926;12(4):835–41.

78. Yang J, Pak YE, Lee TR. Predicting bifurcation angle effect on blood flow in the microvasculature. Microvasc Res [Internet]. 2016;108:22–8. Available from: http://dx.doi.org/10.1016/j.mvr.2016.07.001

79. Pries AR, Secomb TW, Gebner T, Sperandio MB, Gross JF, Gaehtgens P. Resistance to Blood Flow in Microvessels In Vivo.

80. Zweifach BW, Lipowsky HH. Quantitative Studies of Microcirculatory Structure and Function III. Micro vascular Hemodynamics of Cat Mesentery and Rabbit Omentum. Circ Res. 1974;41(3):380–90.

81. Gagnon L, Sakadžic S, Lesage F, Mandeville ET, Fang Q, Yaseen MA, et al. Multimodal reconstruction of microvascular-flow distributions using combined two-photon microscopy and Doppler optical coherence tomography. Neurophotonics [Internet]. 2015;2(1):1–8. Available from: http://neurophotonics.spiedigitallibrary.org/article.aspx?doi=10.1117/1.NPh.2.1.015008

82. Pries AR, Secomb TW, Gaehtgens P. Biophysical aspects of blood flow in the microvasculature ’. 1996;32:654–67.

83. Rocha E Silva M, Braga G, Prist R, Velasco I, Franca E. Physical and physiological characteristics of pressure-driven hemorrhage. Am J Physiol Heart Circ Physiol. 1992;263(5):H1402–10.

84. Courtice FC. The blood volume of normal animals. J Physiol. 1943;102(3):290–305.

85. Gutierrez G, Reines HD, Wulf-Gutierrez ME. Clinical review: Hemorrhagic shock. Crit Care. 2004;8(5):373–81.

86. Troy GC. An overview of hemostasis. Vet Clin North Am Small Anim Pract [Internet]. 1988;18(1):5–19. Available from: http://dx.doi.org/10.1016/S0195-

5616(88)50003-7

87. Granger D, Senchenkova E. Inflammation and the Microcirculation. Morgan & Claypool Life Sciences; 2010.

88. Horsfield K, Woldenberg MJ. Diameters and Cross-Sectional Areas of Branches in the Human Pulmonary Arterial Tree. 1989;251.

89. Suwa N, Niwa T, Fukasawa YS. Estimation of Intravascular Analysis Pressure Gradient Casts by Mathematical of Arterial The First Institute of Pathology , Director : Prof . N . Suwa Tohoku University School of Medicine , Sendai. 1963;168–98.

90. Bark Jr. DL, Para AN, Ku DN. Correlation of Thrombosis Growth Rate to Pathological Wall Shear Rate During Platelet Accumulation. Biotechnol Bioeng. 2012;109(10):2642–50.

91. Li R, Elmongy H, Sims C, Diamond SL. HHS Public Access. 2017;80(3):440–9.

92. Lee MY, Diamond SL. A Human Platelet Calcium Calculator Trained by Pairwise Agonist Scanning. PLoS Comput Biol [Internet]. 2015;11(2):1–24. Available from: http://dx.doi.org/10.1371/journal.pcbi.1004118

93. Kutcher ME, Redick BJ, Mccreery RC, Crane IM, Greenberg MD, Cachola LM, et al. Characterization of platelet dysfunction after trauma. 2013;73(1):13–9.

94. Milisic V, Quarteroni A. ESAIM : Mathematical Modelling and Numerical Analysis ANALYSIS OF LUMPED PARAMETER MODELS FOR BLOOD

FLOW SIMULATIONS AND THEIR RELATION WITH 1D MODELS Vuk Miliˇ si c. 2004;38:613–32.

95. Formaggia L, Nobile F, Quarteroni A, Veneziani A. Multiscale modelling of the circulatory system: A preliminary analysis. Comput Vis Sci. 1999;2(2–3):75–83.

96. Taylor CA, Figueroa CA. Patient-specific Modeling of Cardiovascular Mechanics. Annu Rev Biomed Eng. 2009;11(30):109–34.

97. Quarteroni A, Manzoni A, Vergara C. The Cardiovascular System: Mathematical Modeling, Numerical Algorithms, Clinical Applications. Acta Numer. 2017;26(1):365–590.

98. Gruen R, Brohi K, Schreiber M, Balogh ZJ, Pitt V, Narayan M, et al. Haemorrhage control in severely injured patients. Lancet. 2012;380(9847):1099–108.

99. Gill MR, Reiley DG, Green SM. Interrater Reliability of Glasgow Coma Scale Scores in the Emergency Department. Ann Emerg Med. 2004;43(2):215–23.

100. Cowley A, Ems T, States U. The golden hour in trauma : Dogma or medical folklore ? Injury. 2015;46:525–7.

101. Lundberg SM, Erion GG, Lee S. Consistent Individualized Feature Attribution for Tree Ensembles. arXiv. 2018;(2).

102. Edwards DF, Hollingsworth H, Zazulia AR, Diringer MN. Artificial Neural Networks improve the prediction of mortality in intracerebral hemorrhage. Neurology. 1999;53(2):351–7.

103. Marble RP, Healy JC. A neural network approach to the diagnosis of morbidity outcomes in trauma care. Artif Intell Med. 1999;15:299–307.

104. Karimi H, Bouduhi N. Role of artificial neural networks in prediction of survival of burn patients — a new approach. BURNS. 2002;28:579–86.

105. DiRusso SM, Sullivan T, Holly, C. C, S. N., Savino J. An artificial neural network as a model for prediction of survival in trauma patients: validation for a regional trauma area. J Trauma Acute Care Surg. 2000;2:212–20.

106. Walczak S. Artificial Neural Network Medical Decision Support Tool : Predicting Transfusion Requirements of ER Patients. IEEE Trans Biomed Eng. 2005;9(3):468–74.

107. Mitchell RJ, Ting HP, Driscoll T, Braithwaite J. Identification and internal validation of models for predicting survival and ICU admission following a traumatic injury. Scand J Trauma Resusc Emerg Med. 2018;26(95):1–11.

108. Liu NT, Salinas J. Machine Learning for Predicting Outcomes in Trauma. SHOCK. 2017;48(5):504–10.

109. Ahmed N, Kuo Y, Sharma J, Kaul S. Elevated blood alcohol impacts hospital mortality following motorcycle injury : A National Trauma Data Bank analysis. Injury. 2020;51(1):91–6.

110. Tsiklidis EJ, Sinno T, Diamond SL. Coagulopathy implications using a multiscale model of traumatic bleeding matching macro- and microcirculation. Am J Physiol

Heart Circ Physiol. 2019;l(33).

111. Tsiklidis E, Sims C, Sinno T, Diamond SL. Multiscale systems biology of trauma-induced coagulopathy. Wiley Interdiscip Rev Syst Biol Med. 2018;10(4):1–10.

112. Friedman JH. Greedy Function Approximation: A Gradient Boosting Machine. Ann Stat. 2001;29(5):1189–232.

113. Comittee on Trauma AC of S. NTDB Version 2016. Chicago, IL. 2017;

114. Liu XY, Wu J, Zhou ZH. Exploratory undersampling for class-imbalance learning. IEEE Trans Syst Man, Cybern Part B Cybern. 2009;39(2):539–50.

115. Breiman L. Random Forests. Mach Learn. 2001;5–32.

116. Meredith W, R R, Fakhry S, Emery S, Kromhout-Schiro S. The conundrum of the Glasgow Coma Scale in intubated patients: a linear regression prediction of the Glasgow verbal score from the Glasgow eye and motor scores. J Trauma Acute Care Surg. 1998;44(5):839–825.

117. Lundberg SM, Nair B, Vavilala MS, Horibe M, Eisses MJ, Adams T, et al. Explainable machine-learning predictions for the prevention of hypoxaemia during surgery. Nat Biomed Eng [Internet]. 2018;2(October):749–60. Available from: http://dx.doi.org/10.1038/s41551-018-0304-0

118. Lundberg SM, Lee S. A Unified Approach to Interpreting Model Predictions. Conf Neural Inf Process Syst. 2017;(Section 2):1–10.

119. Shapley L. A Value for n-Person Games. Contrib to Theory Games. 1953;307–17.

120. Pedregosa F, Varoquaux G, Gramfort A, Michel V, Thirion B, Grisel O, et al. Scikit-learn: Machine Learning in Python. J Mach Learn Res. 2011;12(1):2825–30.

121. Zenati MS, Billiar TR, Townsend RN, Peitzman AB, Harbrecht BG. A Brief Episode of Hypotension Increases Mortality in Critically Ill Trauma Patients. J Trauma Inj Infect Crit Care. 2002;(August):232–7.

122. Bhandarkar P, Munivenkatappa A, Roy N, Al. E. On-admission blood pressure and pulse rate in trauma patients and their correlation with mortality: Cushing's phenomenon revisited. Int J Crit Illn Inj Sci. 2017;7:14–7.

123. Eastridge B, Salinas J, McManus J, Blackburn L, Bugler EM, Cooke WH, et al. Hypotension begins at 110 mm Hg: redefining "hypotension" with data. J Trauma Acute Care Surg. 2007;63(2):291–7.

124. Liu X, Wu J, Zhou Z. Exploratory Undersampling for Class-Imbalance Learning. IEEE Trans Syst Man, Cybern Part B. 2009;39(2):539–50.

125. Zhang J, Mani I. kNN Approach to Unbalanced Data Distributions: A Case Study involving Information Extraction. In: Proceeding of International Conference on Machine Learning (ICML 2003), Workshop on Learning from Imbalanced Data Sets. 2003.

126. Fernandez A, Garcia S, Herrera F, Chawla, V. N. SMOTE for Learning from

Imbalanced Data: Progress and Challenges, Marking the 15-year Anniversary. J Artif Intell Res [Internet]. 2018;61:863–905. Available from: https://www.jair.org/index.php/jair/article/view/11192

127. Haldar M, Abdool M, Ramanathan P, Xu T, Yang S, Duan H, et al. Applying deep learning to airbnb search. arXiv e-prints. 2018;1927–35.

128. Johnson AEW, Stone DJ, Celi LA, Pollard TJ. The MIMIC Code Repository: Enabling reproducibility in critical care research. J Am Med Informatics Assoc. 2018;25(1):32–9.

129. Gruber WH, Powell AC, Torous JB. The power of capturing and using information at the point of care. Healthcare [Internet]. 2017;5(3):86–8. Available from: http://dx.doi.org/10.1016/j.hjdsi.2016.09.004

130. Lin L, Xu B, Wu W, Richardson T, Bernal EA. Medical time series classification with hierarchical attention-based temporal convolutional networks: A case study of myotonic dystrophy diagnosis. InCVPR Work. 2019;83–6.

131. Johnson A, Mark RG. Real-time mortality prediction in the Intensive Care Unit. In: AMIA Annu Symp Proc. 2018. p. 994–1003.

132. Harutyunyan H, Khachatrian H, Kale DC, Ver Steeg G, Galstyan A. Multitask learning and benchmarking with clinical time series data. Sci Data [Internet]. 2019;6(1):1–18. Available from: http://dx.doi.org/10.1038/s41597-019-0103-9

133. Tsiklidis EJ, Sims C, Sinno T, Diamond SL. Using the National Trauma Data

Bank (NTDB) and machine learning to predict trauma patient mortality at admission. PLoS One [Internet]. 2020;15(11 November):1–12. Available from: http://dx.doi.org/10.1371/journal.pone.0242166

134. Mobley B, Leasure D. Artificial neural network predictions of lengths of stay on a post-coronary care unit. Heart Lung. 1995;24(3):251–6.

135. Frye K, Izenberg S, Williams M, Luterman A. Simulated biologic intelligence used to predict length of stay and survival of burns. J Burn Care Rehabil. 1996;17(6):540–6.

136. Tsiklidis EJ, Sinno T, Diamond SL. Coagulopathy implications using a multiscale model of traumatic bleeding matching macro- and microcirculation. Am J Physiol Heart Circ Physiol. 2019;317:H73–86.

137. Hirshberg A, Dugas M, Banez EI, Scott BG, Wall MJJ, Mattox KL. Minimizing Dilutional Coagulopathy in Exsanguinating Hemorrhage: A Computer Simulation. J Trauma Inj Infect Crit Care. 2003;54(3):454–63.

138. Chen T, He T, Benesty M, Khotilovich V, Tank Y, Cho H. Xgboost: extreme gradient boosting. R Packag version 04-2. 2015;1(4).

139. Ogunleye A, Wang QG. XGBoost Model for Chronic Kidney Disease Diagnosis. IEEE/ACM Trans Comput Biol Bioinforma. 2020;17(6):2131–40.

140. Slack D, Hilgard S, Jia E, Singh S, Lakkaraju H. Fooling LIME and SHAP: Adversarial Attacks on Post hoc Explanation Methods. In: AAAI/ACM

Conference on Artificial Intelligence, Ethics, and Society (AIES). 2020.